The spherical laser

Experiments on lasing resonances in microspheres compared to Mie theory

by

Peter Zijlstra

Master Thesis
12th May 2005

Complex Photonic Systems (COPS) group
$MESA^+$ **Institute**
Faculty of Science and Technology
University of Twente
Enschede, The Netherlands

Graduation Committee:

Ir. K.L. van der Molen
Dr. A.P. Mosk
Prof. Dr. A. Lagendijk
Dr. R.P.H. Kooyman (BPE)

Abstract

We measured the emission spectrum of dye doped polystyrene microspheres. The microspheres are trapped in optical tweezers to prevent interaction with any surface. Using ethylene glycol the refractive index of the environment is tuned from 1.33 (pure water) to 1.41. We compared the full width at half maximum and TE-TM mode spacing to Mie theory. Our experiments show excellent agreement with the theory.

The classical Mie scattering theory is extended to particles with gain in the refractive index. The extension is found to be invalid beyond a critical size parameter. Beyond the critical size parameter the width of the morphology dependent resonances of the microsphere is negative, which is non-physical. The resonances which have a zero or negative width are lasing resonances.

The emission spectrum of a trapped dye doped polystyrene microsphere immersed in water is also measured using pulsed laser light excitation. The emission spectrum shows multi-mode lasing and a clear threshold is observed. We measured the gain in the refractive index at and above threshold by comparing the experimental results to our extension of the Mie theory. We measured a gain in the refractive index of $\mathrm{Im}(m_I) = 3.9{\cdot}10^{-5}$ for the TE_{95} mode. The gain for the TM_{95} mode is measured to be $5.1{\cdot}10^{-5}$ in the refractive index.

Acknowledgements

This thesis is the result of the work I have done in the group COmplex Photonic Systems (COPS) at the University of Twente. I worked in COPS for almost a year and had a great time during my project and, before my project, the "leerstoelvak".

First of all I would like to thank Karen van der Molen for her enthusiasm and positive guidance during my work. I really appreciate the support and help I got. I would also like to thank Allard Mosk for his support and (almost) infinite many ideas and broad knowledge. Also many thanks to Ad Lagendijk for the discussions on light scattering and the ideas for the theoretical part of my thesis.

I would like to thank Léon Woldering for assistance on the refractive index tuning and the sample preparation. Also thanks to Cock Harteveld for mechanical support and help with the setup. Furthermore I would like to thank the whole COPS group for the good time I had and the pleasant work-atmosphere.

I would like to thank Kees van der Werf (Biophysical Engineering) and Rindert Nauta for their help with the quadrant photo diode, and thanks to Bart van Rooijen with his help on making flow cells. Many thanks to Klaas Smit for making several important parts of the setup. Also thanks to Marileen Dogterom and Astrid van der Horst (AMOLF) for help on the design of the optical tweezers. Furthermore I thank Rob Kooyman (Biophysical Engineering) for being in my graduation committee.

Last but not least I would like to thank my parents and brother for their support during my study. Also thanks to my flatmates for their friendship and the great time I had in Enschede. Finally I would like to thank Linda for her love and support.

Peter Zijlstra
Enschede, May 2005

Contents

List of Figures

List of Tables

Chapter 1

Introduction

Optical microcavities have been studied extensively in recent years. Fluorescent microspheres are widely used in bio-medical applications. Microspheres can act as optical biosensors allowing the identification of a protein attached to it [1]. In a clinical setting blood-flow measurements are performed by injecting fluorescent microspheres in the blood [2].

In fundamental optics and nanophotonics microspheres can also act as high Q resonators in the optical regime (e.g. [3] and references therein). Microspheres can store electromagnetic waves by continuous total internal reflection. If the wave is in phase with itself after one round trip constructive interference results in an enhanced internal field. This is called a whispering gallery mode. The light wave propagates along the circumference of the sphere and is confined near the surface. Early in the 19th century Lord Rayleigh first observed and analyzed sound waves propagating along the walls of the dome in St. Paul's Cathedral in London. He observed sound ("whispers") propagating along the walls and circumfering the dome several times. This is what has been called a whispering gallery mode ever since.

Optical microcavities can have different geometries [3]. Posts, disks, spheres and toroids can serve as high Q cavities. Spherical particles acting as high Q optical resonators are extremely interesting compared to the other geometries. The problem of a light wave scattering on a spherical particle has an exact theoretical solution while this is not the case for the other geometries. Many people have worked on a full solution to the problem of scattering by a sphere. Gustav Mie [4] first worked on the problem of scattering and absorption of electromagnetic waves by spherical particles. Later also Debye and Lorentz contributed to the theory [5]. It is still unclear, however, who first constructed the full solution to the problem and nowadays the theory is referred to as the Mie theory.

The amount of numerical calculations which have to be done to obtain a theoretical

result from the Mie theory is large. As soon as calculations could be computerized an enormous amount of theoretical papers was published. Full treatments of scattering on particles can be found in textbooks [5, 6]. "Active" particles (particles with gain in the refractive index) received a lot of interest in the late 70s because high quality factors of microsphere resonances can be achieved [7–9]. Bennet *et al.* considered absorption in microspheres in order to calculate the effects of heating on the scattering efficiency [10]. Young *et al.* derived asymptotic formulas for the position, width and strength of resonances [11]. Also the effect of perturbations on the shape of the sphere was studied, Lai *et al.* concluded that all qualitative features of the scattered spectrum survive [12].

Experimentally Ashkin was the first to observe whispering gallery mode resonances in the scattered field intensity [13]. He measured the radiation pressure on optically levitated microspheres and observed resonances in the force. He contributed the measured resonances to dielectric surface waves and compared the results to Mie scattering theory. Resonances in polystyrene microspheres were first observed by Benner *et al.* [14] in 1980. In 1998 Holler *et al.* [15] measured spontaneous emission spectra of fluorescent microdroplets. They compared the spectra to a model for the emission of a dipole near a spherical surface, developed by Chew [16, 17].

When a dye doped microsphere is pumped with a high laser power, laser emission can occur at frequencies corresponding to morphology dependent resonances. Lasing in microspherical particles was first reported by Garret *et al.* in 1961. They observed stimulated emission into whispering gallery modes of CaF_2:Sm^{2+} spheres with a diameter of 1 mm. Lasing has also been reported in droplets [18–20], polystyrene microspheres [21] and silica spheres [22, 23]. When a resonance is in a lasing condition stimulated emission results in a drastically increased output power compared to the fluorescent background.

1.1 This thesis

This thesis describes experimental and theoretical research on resonances in dye doped polystyrene microspheres. We are especially interested in laser action in these spheres. The aim of the research performed for this project can be split up in three parts:

1. Measure lasing in a single dye doped polystyrene microsphere. When the quality factor of the microsphere resonance is high and the pump power above threshold, laser lines appear in the emission spectrum of the dye [21]. A threshold can be determined when the output power in the laser line is measured as a function of absorbed pump power.

2. Measure the effect of the environment of a single microsphere on the linewidth and frequency of the resonances. For this purpose the refractive index of the environment is changed and the effect on the natural modes is described and compared to theory.
3. Develop a thorough insight in the Mie theory with gain in the refractive index of the microsphere. In order to do calculations on laser modes in microspheres amplification in the sphere has to be introduced. In theory this can be simulated by introducing a positive imaginary part in the refractive index of the microsphere.

1.2 Outline

In chapter 2 of this thesis theory on spherical cavities with gain will be treated. The Mie scattering theory with gain in the refractive index is studied and the effect of the gain on the results is shown. Also a Fabry Perot cavity with gain in the inside medium is considered. The Fabry Perot model gives more physical insight into the influence of gain on the solution of the Mie theory. Finally a model is discussed which describes the emission of dipoles near a spherical surface. This model allows for direct comparison between theory and the experiments we performed on emission from dye embedded in microspheres.

In chapter 3 we describe the materials and methods used to perform the experiments. The samples are characterized and the apparatus is discussed. Also choices for materials and components are explained. In this chapter we describe the characterization of the optical tweezers. We used the optical tweezers to trap single polystyrene microspheres and move them away from any surface.

The results obtained in the experiments are described in chapter 4. This chapter is split into two parts. Part one (section 4.1) is on the low power continuous wave excitation experiments performed and describes the influence of the environment on the resonances of the microsphere. In part two (section 4.2) the results of the high power pulsed laser light excitation experiments are shown.

The conclusions drawn from this research are listed and discussed in chapter 5. Also recommendations for further research are presented.

Chapter 2

Spherical cavities with gain

In this chapter we discuss the theory on spherical cavities with gain. The mathematical basis of the Mie theory is the subject of section 2.1. Expressions for scattering and absorption cross sections as well as angle dependent scattering functions are given. A reference is made to appendix A which holds the complete derivation of the rigorous solution to the problem. The notation follows Van De Hulst [6] and Bohren and Huffman [5] as much as possible. With respect to the time harmonic factor we follow the convention of van de Hulst ($e^{i\omega t}$). In order to simulate the excitation of a dye doped microsphere gain is inserted in the sphere by means of an imaginary part of the refractive index. This extension of the Mie theory is valid only in the cases of small cavities and low gain .

To develop more physical insight into range of validity of the Mie theory when gain is inserted in the refractive index, in section 2.2 we describe the electromagnetic fields in a Fabry Perot cavity with a complex refractive index.

Finally in section 2.3 we describe the fields resulting from a point dipole oscillating near a spherical interface. This leads to a theory on fluorescence from dipoles embedded in a microsphere. The solution looks very much like the Mie theory and allows us to directly compare theory and experiments.

2.1 Mie theory

The Mie theory describes the scattering of a plane wave by a homogeneous sphere of arbitrary radius. Posing the right boundary conditions at the sphere's surface and at infinity, Maxwell's equations can be solved. Using the spherical symmetry of the problem the fields inside and outside the sphere are expanded in spherical harmonics. The fields are expressed as a series of Legendre polynomials and spherical Bessel functions. The scattering properties of the sphere depend on the size of the sphere and

the refractive indices of the sphere and the surrounding medium. In a homogeneous medium both **E** and **H** satisfy the vector Helmholtz equation:

$$\nabla^2 \overrightarrow{\psi} = -k^2 m_0^2 \overrightarrow{\psi} \tag{2.1}$$

where $k = 2\pi/\lambda$ is the vacuum wave number and m_0 is the (complex) refractive index of the medium.

Posing the right boundary conditions we obtain the solution for an incoming plane wave (expanded in spherical harmonics) being scattered by a sphere of radius a and (complex) refractive index m_I. In order to simplify the calculations the incident radiation is assumed to be linearly polarized (electric field in the x-direction). The incoming wave is propagating along the positive z-axis and is assumed to be periodic with angular frequency ω. The origin of the system of coordinates is the center of the sphere. With respect to the time harmonic factor we adopt the convention of van de Hulst ($e^{i\omega t}$). This means a positive imaginary part of the refractive index indicates amplification (gain). The magnetic permeability is 1.

The following boundary conditions apply at the surface of the sphere:

$$\mathbf{n} \times (\mathbf{E_2} - \mathbf{E_1}) = 0 \tag{2.2}$$

$$\mathbf{n} \times (\mathbf{H_2} - \mathbf{H_1}) = 0 \tag{2.3}$$

where the subscript 1 denotes the sphere and 2 the surrounding medium and **n** is the unit vector normal to the surface of the sphere. In addition the field at infinity needs to go to zero. Solving equation (2.1) in spherical coordinates and posing boundary conditions 2.2 and 2.3 the fields far from the sphere are:

$$E_\theta^{sca} = H_\phi^{sca} = \frac{-i}{kr} e^{-im_0 kr + i\omega t} \cos\phi S_2(\theta) \tag{2.4a}$$

$$-E_\phi^{sca} = H_\theta^{sca} = \frac{-i}{kr} e^{-im_0 kr + i\omega t} \sin\phi S_1(\theta) \tag{2.4b}$$

$$E_r^{sca} = H_r^{sca} = 0 \tag{2.4c}$$

with $S_1(\theta)$ and $S_2(\theta)$ being the scattering amplitude functions:

$$S_1(\theta) = \sum_{n=1}^{\infty} \frac{2n+1}{n(n+1)} [a_n \pi_n(\cos\theta) + b_n \tau_n(\cos\theta)] \tag{2.5}$$

$$S_2(\theta) = \sum_{n=1}^{\infty} \frac{2n+1}{n(n+1)} [b_n \pi_n(\cos\theta) + a_n \tau_n(\cos\theta)] \tag{2.6}$$

where n is the mode number.

The angle dependent functions π_n and τ_n are functions of the P_n^1 Legendre polynomials:

$$\pi_n(\cos\theta) = \frac{1}{\sin\theta} P_n^1(\cos\theta) \tag{2.7a}$$

$$\tau_n(\cos\theta) = \frac{d}{d\theta} P_n^1(\cos\theta) \tag{2.7b}$$

The coefficients a_n and b_n are the scattering coefficients:

$$a_n = \frac{m_0\psi_n'(y)\psi_n(x) - m_I\psi_n(y)\psi_n'(x)}{m_0\psi_n'(y)\zeta_n(x) - m_I\psi_n(y)\zeta_n'(x)} \tag{2.8}$$

$$b_n = \frac{m_I\psi_n'(y)\psi_n(x) - m_0\psi_n(y)\psi_n'(x)}{m_I\psi_n'(y)\zeta_n(x) - m_0\psi_n(y)\zeta_n'(x)} \tag{2.9}$$

where the variable $x = m_0 ka$ is the size parameter of the system and $y = m_I ka$. The prime denotes differentiation with respect to the argument. The size parameter and y determine the scattering properties of the sphere. Note that, as we expect, the scattering coefficients and thus the scattered field disappear if there is no particle present ($m_I = m_0$). ψ_n and ζ_n are the Riccati Bessel functions which are defined as:

$$\psi_n(z) = z j_n(z) = \sqrt{\frac{\pi}{2z}} J_{n+\frac{1}{2}}(z) \tag{2.10a}$$

$$\chi_n(z) = -z n_n(z) = \sqrt{\frac{\pi}{2z}} Y_{n+\frac{1}{2}}(z) \tag{2.10b}$$

$$\zeta_n(z) = z h_n^{(2)}(z) = \psi_n(z) + i\chi_n(z) \tag{2.10c}$$

where $h_n^{(2)}(z)$ is the outgoing spherical Hankel function, with the following asymptotic behavior for large z:

$$h_n^{(2)}(z) \approx \frac{i^{n+1} e^{-iz}}{z} \tag{2.11}$$

The dimensionless efficiency factor Q is defined as the ratio of the optical cross section (C) and the geometrical cross section (G) and can be written as:

$$Q_{ext} = \tfrac{C_{ext}}{G} \ , \ Q_{sca} = \tfrac{C_{sca}}{G} \ , \ Q_{abs} = \tfrac{C_{abs}}{G}$$

where, by definition,

$$Q_{ext} = Q_{sca} + Q_{abs}. \tag{2.12}$$

The extinction and scattering efficiencies can be written as a function of $S_1(\theta)$ and $S_2(\theta)$:

$$\begin{aligned} Q_{ext} &= \frac{4}{x^2} Re[S(0)] \\ &= \frac{2}{x^2} \sum_{n=1}^{\infty} (2n+1) Re(a_n + b_n) \end{aligned} \tag{2.13}$$

$$\begin{aligned} Q_{sca} &= \frac{1}{\pi a^2 m_0^2 k^2} \int_0^{\pi} \int_0^{2\pi} (|S_1(\theta)|^2 \cos^2(\phi) + |S_2(\theta)|^2 \sin^2(\phi)) \sin(\theta) d\phi d\theta \\ &= \frac{2}{x^2} \sum_{n=1}^{\infty} (2n+1)(|a_n|^2 + |b_n|^2) \end{aligned} \tag{2.14}$$

The absorption efficiency follows from equation (2.12) now. A complete derivation of the amplitude functions as well as the scattering and extinction efficiencies can be found in Appendix A.

Fig. 2.1 shows the scattering efficiency for a polystyrene sphere in water ($m_0 = 1.33$) for (a) a real and (b) a complex refractive index (gain) plotted as a function of radius a (in units $1/m_0 k$). The insets show a segment enlarged.

As can be seen from the insets in Fig. 2.1 the scattering efficiency has a pronounced ripple structure. The peaks emerge in the spectrum as a result of the resonances in the scattering coefficients a_n and b_n. The denominators of a_n and b_n are a function of spherical Bessel functions, therefore a_n and b_n have poles at a certain complex size parameter. Each a_n and b_n has an infinite number of poles. These poles are the natural modes of the sphere.

The sharp resonant peaks are the result of whispering gallery modes inside the sphere. Light in such modes is trapped near the surface by total internal reflection and travels around the surface of the sphere. Each resonant mode number n has infinite orders but only the first order is observed in the scattering efficiency because the second and higher orders are broader than the free spectral range. Exceptions are very high mode numbers above $n = 150$ where the width of second order resonances is smaller than the free spectral range.

The much broader maxima and minima in the scattering efficiency are due to interference between the scattered and the diffracted electromagnetic wave [6]. The diffracted electromagnetic wave is the result of Fraunhofer diffraction. Therefore it depends on the size of the particle but not on its composition. The maxima are a result of constructive interference while the minima occur due to destructive interference.

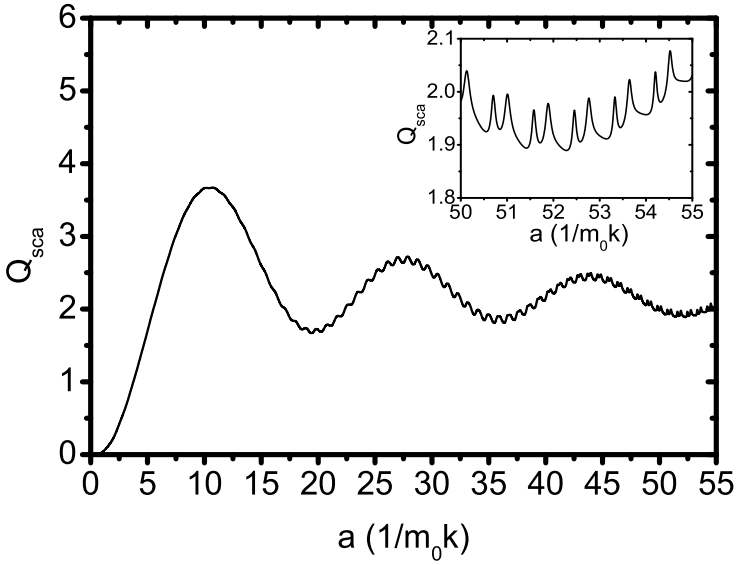

(a)

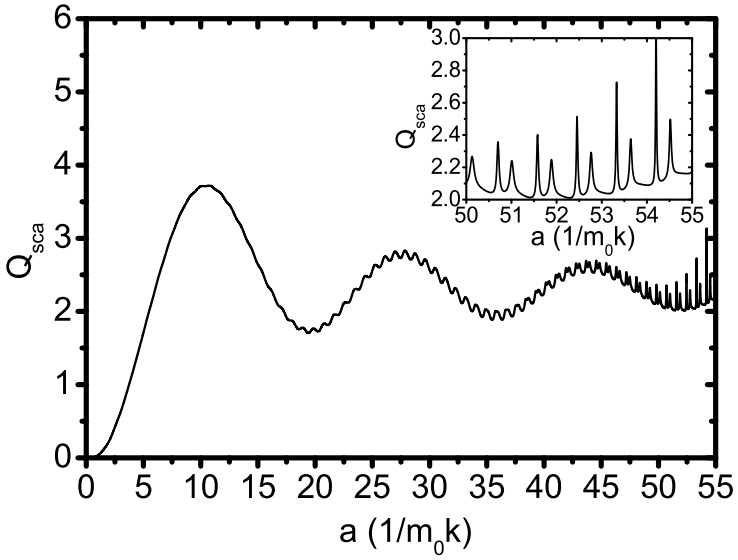

(b)

FIG. 2.1: Scattering efficiency for a sphere in water as a function of radius a (in units $1/m_0k$). (a) $m_I = 1.59$ and (b) $m_I = 1.59 + 0.001i$. The insets show a segment enlarged.

As can be seen from Fig. 2.1 the resonances always appear in pairs, the transverse magnetic (TM) and transverse electric (TE) mode. A TE mode has no radial electric field component so the electric field vector is parallel to the surface of the sphere. TM modes have no radial magnetic field component. The TE-TM mode spacing results from a different coefficient for total internal reflection for TE and TM modes. This results in a different phase shift upon internal reflection which leads to the TE-TM mode spacing. As the mode number increases so will the TE-TM mode spacing, the

mode number being the number of internal reflections. A pole in the a_n coefficient gives rise to a TM mode while a pole in b_n defines the TE modes [5]. TE modes are the narrower of the two. This is because the coefficient for total internal reflection in the sphere is higher which gives rise to a higher resonance quality factor.

The derivation of the efficiency factors seems to hold for both real and complex refractive index of the sphere. There seem to be no restrictions as to which values m_I can have. However when gain is inserted in the refractive index of the sphere a problem arises when the boundary conditions are applied and the scattering coefficients calculated. The scattering coefficients are calculated from a system of linear equations (c_n and d_n are the coefficients for the field inside the sphere):

$$\psi_n^{'}(x) - a_n\zeta_n^{'}(x) = c_n\psi_n^{'}(y) \tag{2.15a}$$
$$m_0[\psi_n(x) - a_n\zeta_n(x)] = m_I c_n\psi_n(y) \tag{2.15b}$$
$$\psi_n(x) - b_n\zeta_n(x) = d_n\psi_n(y) \tag{2.15c}$$
$$m_0[\psi_n^{'}(x) - b_n\zeta_n^{'}(x)] = m_I d_n\psi_n^{'}(y) \tag{2.15d}$$

Cramer's rule states that the system of linear equations (2.15) has a unique and non-singular solution if the determinant (which is equal to the denominator of the scattering coefficients) is non-zero. When this is not the case the solution is singular and the scattering coefficients have a complex pole. The value of the coefficients a_n and b_n is infinity which mathematically means an electromagnetic field of infinite amplitude. Physically the sphere has a morphology dependent resonance (MDR) for this particular complex size parameter and mode number n. The real part of this size parameter x_0 gives the spectral position of the resonance (combination of wavelength and sphere size) and the imaginary part defines the width of the resonance:

$$\Gamma = 2\ \mathrm{Im}(x_0) \tag{2.16}$$

Fig. 2.2 shows the width of the first-order resonance as a function of mode number in a microsphere of 10.6 μm in diameter. Both TE and TM polarization are plotted. Fig. 2.2 (a) shows the widths for a polystyrene sphere ($m_I = 1.59$) in water ($m_I = 1.33$). In Fig. 2.2 (b) the polystyrene sphere has gain in the refractive index, indicated by the imaginary part ($m_I = 1.59 + 0.001i$). The insets show a segment enlarged. When the sphere has gain in the refractive index, the width of the first-order resonance becomes negative at a certain mode number. At and beyond the size parameter at which this mode is resonant the solution of the Mie theory is non-physical. All higher mode numbers will also have a negative width and therefore also give a non-physical solution beyond their resonant size parameter.

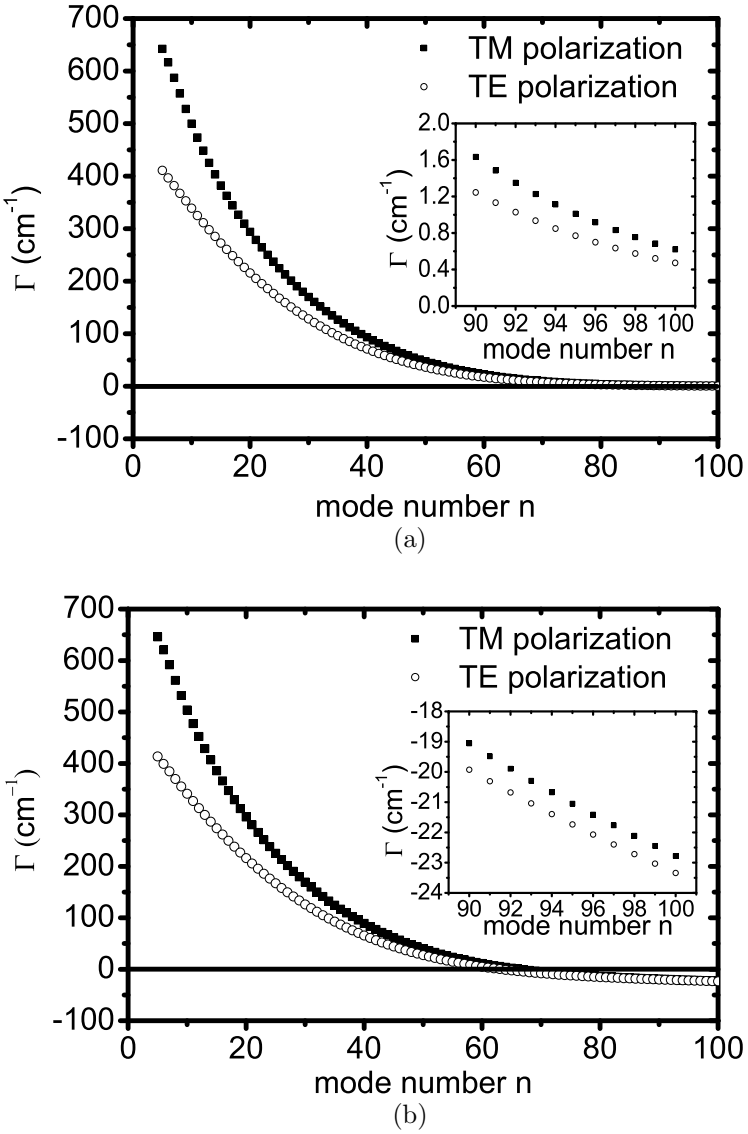

FIG. 2.2: Width of the first-order resonance as a function of mode number for a microsphere of 10.60 μm in diameter immersed in water ($m_0 = 1.33$) for (a) $m_I = 1.59$ and (b) $m_I = 1.59 + 0.001i$ (gain). The insets show a segment enlarged.

In the case of a refractive index of $m_I = 1.59 + 0.001i$ the TE resonance with mode number 63 (TE_{63}) is the first mode with a negative width. This mode occurs at $x \approx 57.7$ so the Mie theory cannot be extended beyond this size parameter for this combination of parameters. This limit to the validity of the Mie theory is often overlooked and gives rise to a wrong interpretation of both theory and experiments. Earlier attempts to interpret the Mie theory with gain in the refractive index lead to unphysical results [8, 9, 24].

Calculating the width of the resonances makes it possible to determine the lasing

threshold for a certain sphere size and gain. The lasing threshold will be reached when a mode number has width zero. As mentioned before TE modes are narrower than TM modes and therefore have a lower lasing threshold. When a certain mode is in a lasing condition higher mode numbers will automatically be lasing modes. This is because higher mode numbers will have a higher resonance quality factor. In the previous discussion the gain in the refractive index is assumed to be frequency independent. In experiments however only a limited number of modes will show lasing due to the gain being frequency dependent.

More insight in this complex problem of spheres with gain can be obtained by studying a much simpler system. A Fabry Perot cavity is mathematically easy to understand and gives a more didactic view on what happens in the theory and summations when gain is inserted in the refractive index. Therefore a Fabry Perot cavity with gain will be described in the next section.

2.2 A Fabry Perot cavity with gain

A simple 2-dimensional Fabry Perot cavity with gain in the refractive index is studied. The cavity transmission will be derived. This will help interpret the non-physical solution we find for spheres with gain in the Mie theory. The Fabry Perot cavity

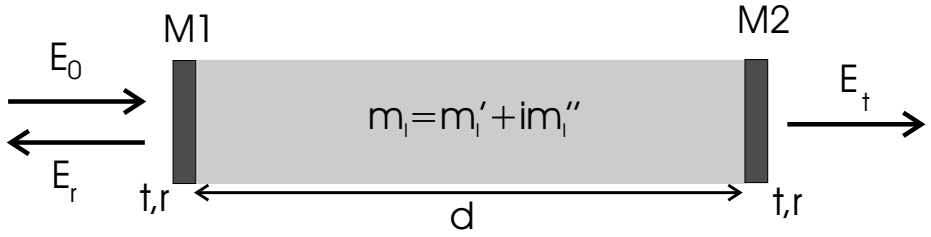

FIG. 2.3: Fabry Perot cavity with a gain medium in between two mirrors (M1 and M2) at distance d. The incoming wave has an amplitude E_0, whereas the outgoing waves have an amplitude E_t and E_r. Both mirrors have the same transmission and reflection coefficients (t and r).

considered consists of 2 identical semitransparent mirrors M1 and M2. The mirrors are at distance d of each other. The refractive index in between the mirrors is m_I where m_I can be a complex number (absorption and gain are allowed). In an experiment the gain medium could be a pumped dye solution. See Fig. 2.3 for a schematic of the considered system.

2.2.1 Model

The transmission and reflection of the cavity is modeled by analyzing the subsequent transmitted waves through the system [25]. We allow the incoming wave to transmit through the first mirror without reflection. Start with the incoming wave which is transmitted once and amplified by the medium:

$$E_{t1} = E_0 t e^{-ikm_I d} \tag{2.17}$$

where t is the transmission coefficient, k is the wavenumber in vacuum, m_I is the refractive index of the medium and d is the distance between the mirrors. The wave which reflects 2 times contributes:

$$E_{t2} = E_0 t r^2 e^{-3ikm_I d} \tag{2.18}$$

and so forth. Adding all reflections gives:

$$\begin{aligned} E_t &= \sum_{N=1}^{\infty} E_0 t r^{(2N-2)} e^{-i[\frac{2\pi}{\lambda_0} m_I d(2N-1)]} \\ &= \sum_{N=1}^{\infty} E_0 t e^{i\frac{2\pi}{\lambda_0} md} r^{2(N-1)} e^{-i[\frac{4\pi}{\lambda_0} m_I d](N-1)} \end{aligned} \tag{2.19}$$

From here there are two possible routes to the final solution: one is to make this sum into an finite sum of the lower order reflections. In case of gain in the system higher order reflections will always have a bigger amplitude than previous reflections and therefore give a significant contribution. The second option is to take into account all reflections and make an infinite sum over all reflections. The latter is the method used in Mie theory and therefore will be adopted here as well.

Evaluating the summation leads to a geometric series which converges to

$$E_t = E_0 t e^{i\frac{2\pi}{\lambda_0} m_I d} \frac{1}{1 - r^2 e^{-i[\frac{4\pi}{\lambda_0} m_I d]}} \tag{2.20}$$

with the strict condition that

$$a = |r^2 e^{i[\frac{4\pi}{\lambda_0} m_I d]}| < 1 \tag{2.21}$$

The ratio of the series a depends on both the refractive index in the cavity and the cavity size. Using the above formalism the transmission through a Fabry Perot cavity can be analyzed for any combination of parameters as long as inequality (2.21) is obeyed. However, if (2.21) is not fulfilled, the sum (2.19) does not converge, and the result (2.20) is unphysical.

Now consider a cavity with identical equal mirrors ($r = 0.99$) and a medium in between the mirrors ($m = 1.5 \pm in'$) where the sign of n' determines whether the medium has gain or absorption. Now compare two situations: $m = 1.5$ (Fig. 2.4) and $m = 1.5 + 0.002i$ (gain, Fig. 2.5).

In all calculations the incident vacuum wavelength is 600 nm. For each of these situations the relative transmission of intensity through a cavity for cavity lengths varying from 0 to 1200 nm is plotted (Figs. 2.4 (a) and 2.5 (a)). Also the variable a given in equation (2.21) is examined (Figs. 2.4 (b) and 2.5 (b)).

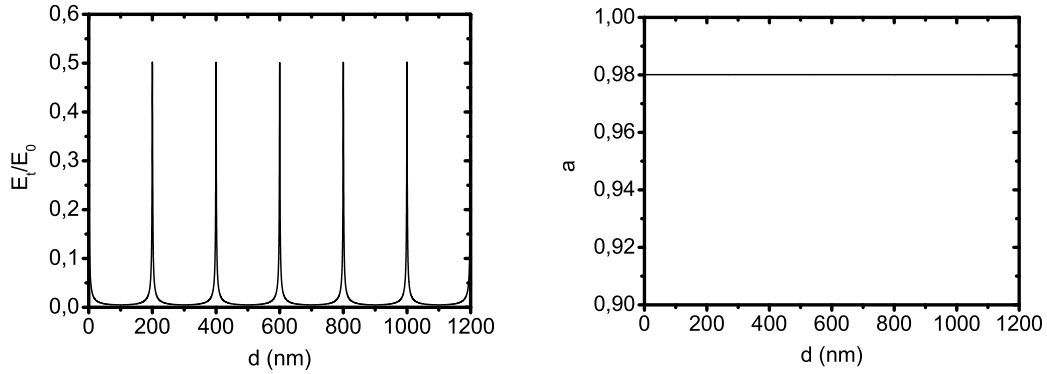

(a) (b)

FIG. 2.4: (a) Relative transmitted electric field through a 2-dimensional Fabry Perot cavity of length d. The incident field has a wavelength of 600 nm and the refractive index inside the cavity is 1.5. (b) Variable a for the same cavity as a function of cavity size.

As can be seen from figs. 2.4 (b) and 2.5(b) the condition given in formula 2.21 is not satisfied in the case of a positive imaginary part of the refractive index (gain). The value of a exceeds one at a critical cavity size of about 480 nm. At this cavity size the sum over an infinite number of reflections (equation (2.19)) is not converging anymore. The solution as given in formula 2.20 is correct for cavities having $a < 1$ and incorrect for all other cavities.

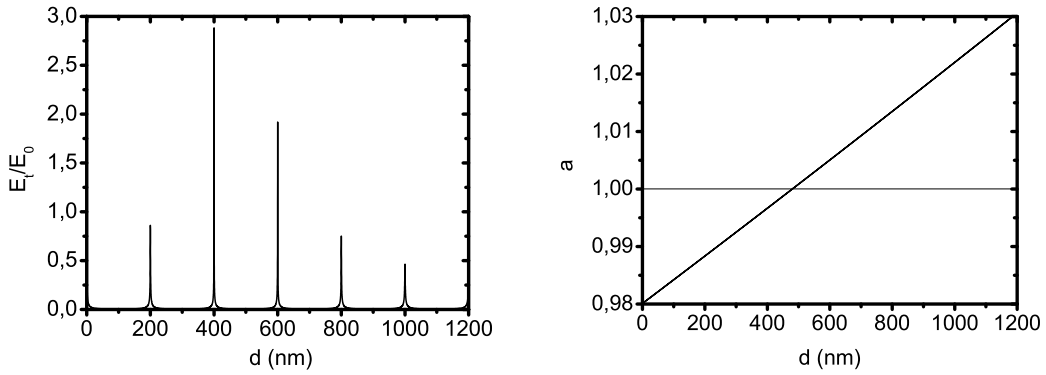

(a) (b)

FIG. 2.5: (a) Relative transmitted electric field through a 2-dimensional Fabry Perot cavity of length d. The incident field has a wavelength of 600 nm and the refractive index inside the cavity is 1.5+0.002i. (b) Variable a for the same cavity as a function of cavity size.

Comparison to Mie theory leads to the conclusion that in Mie theory a summation over infinitely many reflections at the sphere surface is done implicitly. This is done when the coupling equations (2.15) are solved in the same way as done for the Fabry Perot cavity. Summing over infinitely many incoming and outgoing waves explicitly would lead to the same solution as given in section 2.1. Again the condition for the coefficient a remains and the theory would be invalid for systems having $a > 1$. In the Mie theory the equivalent situation (where in the Fabry Perot model $a = 1$) occurs at the complex size parameter at which the width of a mode becomes negative.

2.3 Fluorescence from a dipole near a spherical interface

In the experiments described in this thesis fluorescence from dye embedded in microspheres has been studied. As can be seen from Fig. 2.6 there is a conceptual difference between (a) scattering on a microsphere and (b) emission from dye inside a microsphere. In the case (a) an incoming plane wave excites the modes inside the sphere and the outgoing field is a superposition of the incoming plane wave (expanded in spherical harmonics) and the scattered spherical wave. Case (b) however involves sources inside a microsphere which emit photons without phase relation to the pump source. These photons excite the modes of the microsphere from the inside.

In order to compare experiments to theoretical results a model for the fluorescence of atoms inside a microsphere is needed. A theoretical description of this problem has been developed by Chew and coworkers [16,17,26]. In these papers the electromagnetic

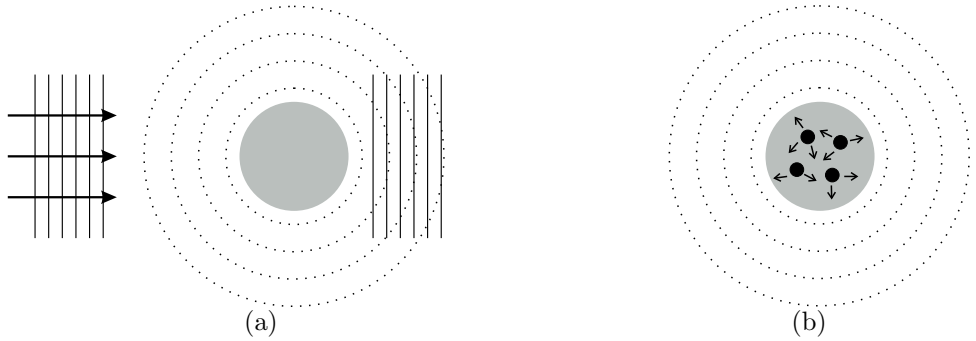

FIG. 2.6: Conceptual difference between (a) scattering and (b) emission problems. In scattering theory an incoming plane wave is scattered by a sphere. The resulting field is a superposition of the incoming wave and the scattered wave. Fluorescence theory describes the field resulting from oscillating dipoles in a sphere which emit photons with a random phase.

fields outside the sphere, the total radiated power and the transition rates of atoms inside and outside a spherical particle are studied. Here the expressions from these papers will be stated and results will be shown.

Consider a spherical particle of arbitrary radius a. The refractive index of the particle is referred to as m_I and of the outside medium as m_0. The total radiated power R due to a dipole $\mathbf{p}$ at position $\mathbf{r}'$ ($\mathbf{r}'$ inside the sphere) radiating at frequency ω is evaluated for radial and tangential dipole orientation. The total radiated power is normalized to the radiation rate in the bulk medium m_0. The notation is adapted to fit the notation used previously in this thesis. Hence, for a dipole oscillating in the radial direction (equation (10) in [16])

$$\frac{R^{\perp}}{R_0^{\perp}} = \frac{1}{2}\frac{m_I}{m_0^3}\frac{ck_0^2}{a^2}\sum_{n=1}^{\infty} n(n+1)(2n+1)\frac{j_n^2(y_1)}{y_1^2|D_n|^2} \tag{2.22}$$

and for tangential oscillations (equation (11) in [16])

$$\frac{R^{\parallel}}{R_0^{\parallel}} = \frac{1}{4}\frac{m_I}{m_0^3}\frac{ck_0^2}{a^2}\sum_{n=1}^{\infty}(2n+1)\left(\left|\frac{[y_1 j_n(y_1)]'}{y_1 D_n}\right|^2 + \frac{1}{m_0^2 m_I^2}\frac{j_n^2(y_1)}{|D_n'|^2}\right) \tag{2.23}$$

where $y_1 = m_0 k r'$ with k the wavenumber in vacuum and r' the coordinate at which the dipole radiates. The factors D_n and D_n' are given by

$$D_n = m_I^2 j_n(y)[x h_n^{(2)}(x)]' - m_0^2 h_n^{(2)}(x)[y j_n(y)]' \tag{2.24a}$$
$$D_n' = j_n(y)[x h_n^{(2)}(x)]' - h_n^{(2)}(x)[y j_n(y)]' \tag{2.24b}$$

where $x = m_0 ka$ and $y = m_I ka$. Note that the denominators of a_n and b_n are equal to D_n and D'_n. This is as we expect, the resonant modes in both theories should be the same.

To calculate the emission from a microsphere which contains a certain homogeneous concentration of dye molecules equations (2.22) and (2.23) should be integrated over the volume of the microsphere. Also the field of the radial and tangential oriented dipoles should be weighted so the resulting power is an average over random oriented dye molecules. In order to achieve this we perform the an integral over the volume of the sphere [17]:

$$\frac{R}{R_0} = \int (\frac{1}{3}\frac{R^{\perp}}{R_0^{\perp}} + \frac{2}{3}\frac{R^{\parallel}}{R_0^{\parallel}}) d^3V = 4\pi \int (\frac{1}{3}\frac{R^{\perp}}{R_0^{\perp}} + \frac{2}{3}\frac{R^{\parallel}}{R_0^{\parallel}})(r')^2 dr' \tag{2.25}$$

We evaluate the integral in equation (2.25) numerically as a weighted summation.

Fig. 2.7 shows the radiated power (equation (2.25)) as a function of size parameter for (a) real and (b) complex refractive index (gain). The radiated power from the sphere filled with dye molecules is normalized to the power radiated by the same number of dye molecules in bulk material of refractive index m_0 and is an average over all dye molecules. The insets show a segment enlarged. As expected the ripple structure due to the natural modes is the same as in the Mie theory.

As can be seen in Fig. 2.7 the average spontaneous emission rate at the frequency of a natural mode of the sphere is enhanced compared to the bulk value. In a cavity the spontaneous emission rate is determined by the local density of states (LDOS). The LDOS counts the available number of electromagnetic modes in which photons can be emitted. Naturally a high LDOS implies an enhanced spontaneous emission rate. The LDOS strongly depends on location of the emitter in the cavity and the emission frequency. Emission at natural frequencies of the cavity will be strongly confined to the surface of the sphere where the LDOS can be a factor of several thousands higher than for the bulk medium depending on the mode number. Modes which are confined to the surface of the sphere are called whispering gallery modes (WGM). All natural modes of first order in a spherical cavity are whispering gallery modes except for the lower mode numbers (below mode number 5) which have a mode volume that is not confined to the surface of the sphere.

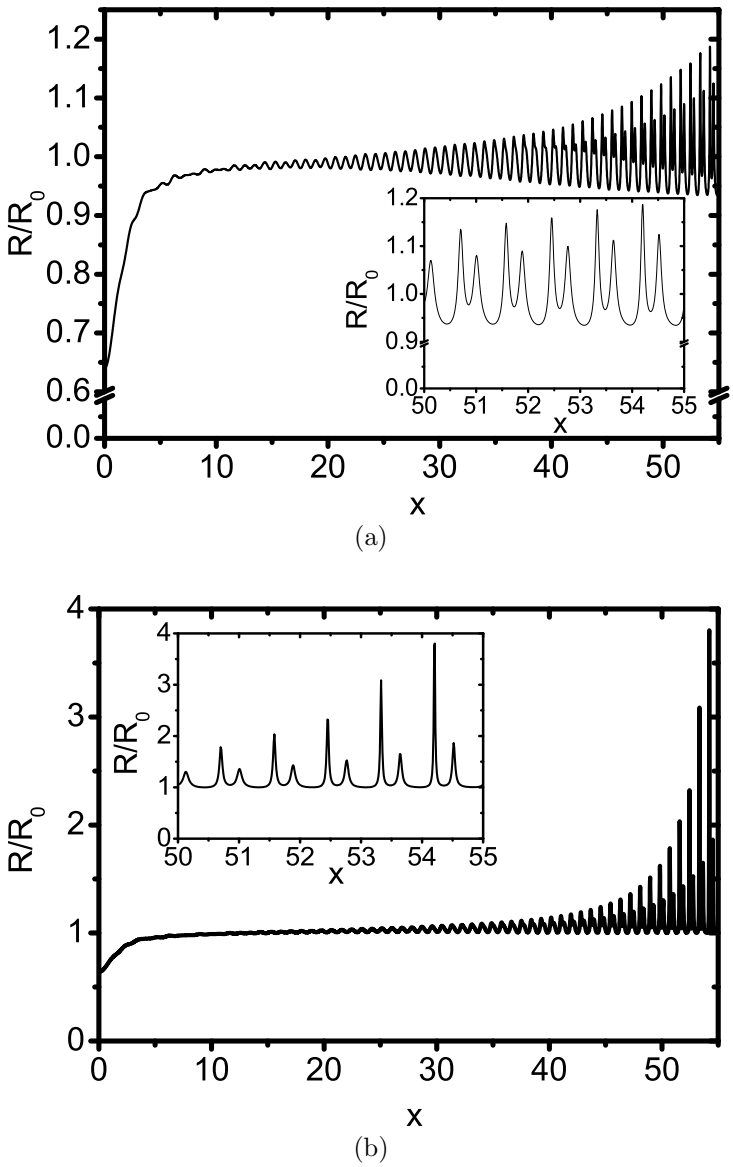

FIG. 2.7: Averaged radiation power of a homogeneous concentration of fluorescent dipoles in a spherical particle immersed in water ($m_0 = 1.33$). Refractive indices of the particle are (a) $m_I = 1.59$ and (b) $m_I = 1.59 + 0.001i$ (gain). The insets show a segment enlarged.

At frequencies which are off resonance the spontaneous emission rate is lower than the radiation in a bulk medium with refractive index m_0. At these frequencies the spontaneous emission rate is inhibited. This is the result of the average local density of states in the sphere being lower than the value for the bulk medium.

Note again that the values in Fig. 2.7 are averaged over all dye molecules and that the LDOS and thus the local spontaneous emission rates can exceed these values by a

factor of several thousands for high order modes and dye molecules near the surface. However these modes have a very low mode volume so on average over all dye molecules the spontaneous emission rate will not reach these values.

The main difference between the Mie scattering theory and the fluorescence from atoms is the conceptual difference between scattering and emission as shown in Fig. 2.6. In the Mie theory an incoming plane wave is scattered by a spherical particle. The resulting field is a superposition of the incoming and scattered wave and therefore shows interference fringes in the scattering efficiency (see Fig. 2.1). In experiments the excitation of the dye in the microsphere is done from the outside by laser light. However the excitation of the natural modes of the sphere is from the inside by the fluorescence of the dye molecules. After filtering out the pump light only the fluorescence of the dye molecules is measured. Therefore the theory on fluorescence of molecules in spherical cavities allows for a quantitative comparison between experiments and theory, which is not possible using the Mie theory. In some cases [14] a comparison between the Mie scattering cross section and emission from dye embedded in spherical particles is made. This comparison is correct for the identification of the modes because the mode structure is identical. A quantitative analysis however is impossible because the interference between the Fraunhofer diffracted and the scattered wave, as well as the background are different.

The denominators in the field expressions of the Mie scattering (section 2.1) and the fluorescence model (section 2.3) are the same. When introducing gain in the refractive index of the microsphere the width of the resonances will become negative eventually for increasing cavity size or gain. At and beyond the size parameter at which the first resonance has a negative width *both* models are unphysical. Therefore fitting experimental data with pump powers above threshold is not meaningful.

Chapter 3

Materials and methods

The aim of the work described in this thesis is to measure emission from dye embedded in polystyrene microspheres. Especially the natural modes of the microsphere are interesting features of the spectrum. In order to measure these very narrow resonances we need a single microsphere, far away (several times the diameter) from any surface. For an isolated microsphere the spherical symmetry is not perturbed and a full and analytical theory can be used.

Optical tweezers are used to lift a single microsphere from the surface of the sample holder. Optical tweezers use light induced forces to lift a microsphere in a fluid and prevent interaction of the microsphere with any kind of surface. An Intensified Charge-Coupled Device (ICCD) attached to a high resolution spectrograph is used for the detection of the emitted light. This detection system combines the high resolution needed to detect the narrow natural modes of the microsphere with the light sensitivity that we need to detect emission from a single microsphere.

In this chapter we address the materials and methods used to measure the spectra of single microspheres. In section 3.1 the samples and the sample preparation are discussed. We describe the microspheres and characterize the emission spectrum. In section 3.2 we show the setup used in the experiments. Finally, in section 3.3 we describe the characterization of the optical tweezers. Some theory is addressed as well as measurements which have been performed to characterize the tweezers.

3.1 Samples and sample preparation

The samples used in the experiments consist of a suspension of dye doped polystyrene microspheres in a borosilicate glass capillary (inside dimensions 0.1 mm by 2 mm by 40 mm, glass thickness 0.1 mm). The microspheres are obtained from Duke Scientific Corporation (catalogue number G1000) and have a specified mean diameter of 10.1

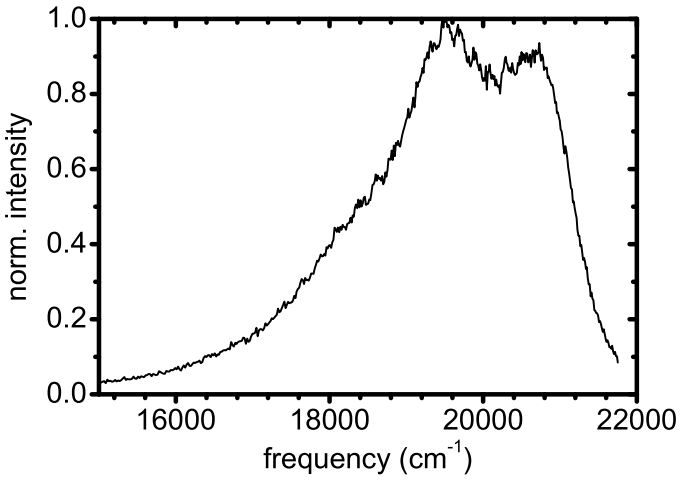

FIG. 3.1: Emission spectrum of an ensemble of 10.1 μm diameter dye doped polystyrene microspheres. The emission maximum is at 19500 cm^{-1} while the excitation maximum is at 21370 cm^{-1}

μm with a specified size dispersion of 5 % (standard deviation). The spheres are composed of polystyrene doped with an unknown dye which emits in the green part of the spectrum. The spectrum, as shown in Fig. 3.1, has width of 50 nm with the emission peak at 515 nm (19500 cm^{-1}). The specified excitation maximum is 468 nm (21370 cm^{-1}), implying a Stokes shift of about 47 nm. The specified estimated quantum efficiency of the dye is 60%. The specified concentration of the dye in the microsphere is about 2% by weight of polystyrene. The dye is mixed with the polymer during the production process which results in a homogeneous dye concentration throughout the microsphere. Leakage of the dye into the solution is excluded as the dye is incorporated in the polymer matrix. As the dye emission spectrum has its maximum around 515 nm, all the measurements described in this thesis were performed in this region. This ensures the highest possible signal. At 510 nm the refractive index of pure polystyrene is 1.60 $\pm$0.005 at 293 K [27, 28]. As the microspheres have around 2 % dye embedded a deviation of order 1 % in the refractive index is to be expected.

Most of our measurements are performed on microspheres in water (m_0 = 1.3332 at 293 K and 589 nm). Water is one of the lowest-refractive-index solvents available. So by using water we obtain the highest possible contrast in index of refraction and therefore the best possibilities of seeing the morphology dependent resonances (MDR) of the microspheres. All samples used have a sphere concentration of $10^5/cm^3$. At this concentration we have a reasonable amount of spheres in the glass capillary (30-50 microspheres) but no spheres stick to each other.

fraction water	*nD (293K)*	*nD (298K)*
1.0	1.3332	1.3325
0.8	1.3554	1.3544
0.6	1.3760	1.3751
0.4	1.3992	1.3978
0.2	1.4148	1.4131
0.0	1.4317	1.4302

Table 3.1: Refractive indices of mixtures of water with ethylene glycol measured at 589 nm. The refractive indices were measured at a temperature of 293 and 298 K and are shown as a function of the volume fraction of water.

The full width half maximum and TE-TM mode spacing of the microspheres is measured as a function of index contrast. For this purpose a series of measurements is done in which the refractive index of the surrounding medium is tuned. The tuning of the refractive index is achieved by mixing water with ethylene glycol ($m_0 = 1.4317$ at 293 K and 589 nm) in various fractions. Ethylene glycol does not chemically affect polystyrene. Therefore we can be sure the microspheres do not deform which would substantially lower the microsphere resonance quality factor. Ethylene glycol is miscible with water in all volume fractions so all refractive indices between 1.3332 and 1.4317 can be obtained.

Refractive indices of the mixtures are measured with an Abbe refractometer type 1T which is temperature stabilized and has an accuracy of 0.0002 in refractive index. Table 3.1 shows the volume fractions of water and ethylene glycol used and the refractive index measured at both 293 and 298 K. The refractive indices are measured at 589 nm while the spectra are measured around 515 nm. As the dispersion of water is small over this wavelength range [29] the change in refractive index of the mixtures is assumed to be less than 0.005.

For every measurement performed a different microsphere is excited. This gives a distribution of experimental results due to the variation in diameter of the microspheres (5 %, specified by Duke Scientific Corporation) because the spectral position of a specific mode number depends on sphere size. This is not a problem in the experiments because within the spectral range of the spectrograph the same mode numbers are observed in the spectra. As we want to compare mode numbers instead of spectral positions of resonances this does not limit us in the experimental work.

3.2 Apparatus

Fig. 3.2 shows the setup which is used to excite the polystyrene microspheres and measure the spectra. The excitation, detection and the optical tweezers beam paths pass through the microscope, which is a Nikon Eclipse TE2000-U inverted microscope. The apparatus consists of three parts each having its own function. Section 3.2.1 describes the two different light sources used to excite the dye in the microspheres. In section we 3.2.2 continue on the detection system used to measure the emission spectrum of the dye in a single microsphere. Optical tweezers were used to trap a single microsphere and lift it from the glass surface of the capillary. In section 3.2.3 we describe the optical tweezers used in the experiments.

3.2.1 Excitation

We used two light sources to excite the dye in the microspheres. A Spectra Physics continuous wave Argon laser (Satellite 2016) at 488 nm which was used for low power continuous wave (CW) excitation. The maximum output power of the laser is 30 mW at 488 nm. The second laser we used is an Nd:Yag pumped optical parametric oscillator (OPO). The OPO source is a Coherent Infinity-XPO and is tunable in the range of 450 nm to 1064 nm. The pulse duration is about 3 ns (depending on emission wavelength) with a repetition rate of 50 Hz. The pulse energy is about 10 mJ per pulse, which is attenuated by a factor of 10.000 by two Glan laser prisms. We used the OPO source at 470 nm because this is the maximum in the excitation spectrum of the dye in the microspheres (section 3.1). Excitation at this wavelength ensures a high excitation efficiency.

3.2.2 Detection

The detection system consists of an Oriel Instruments spectrograph (type MS257) with an Intensified Charge-Coupled Device (ICCD, Princeton Instruments ICCD 576) camera attached to it. The grating in the spectrograph has 1200 lines and has a pixel size of 0.0227 nm per pixel at 515 nm with a range of 10 nm. Considering cross talk between neighboring pixels the resolution of the spectrograph is about 0.08 nm. The ICCD camera is cooled to 243 K by means of a Peltier element. A photon counting sensitivity with a 10 % quantum efficiency is specified, so the ICCD is capable of detecting very low intensity.

3.2.3 Optical tweezers

The laser used to trap single microspheres is a Laser Quantum Ventus continuous wave Nd:Yag laser emitting at 1064 nm with a maximum power of 3.5 watt in a single transversal mode. Polystyrene is transparent at 1064 nm so light at this wavelength

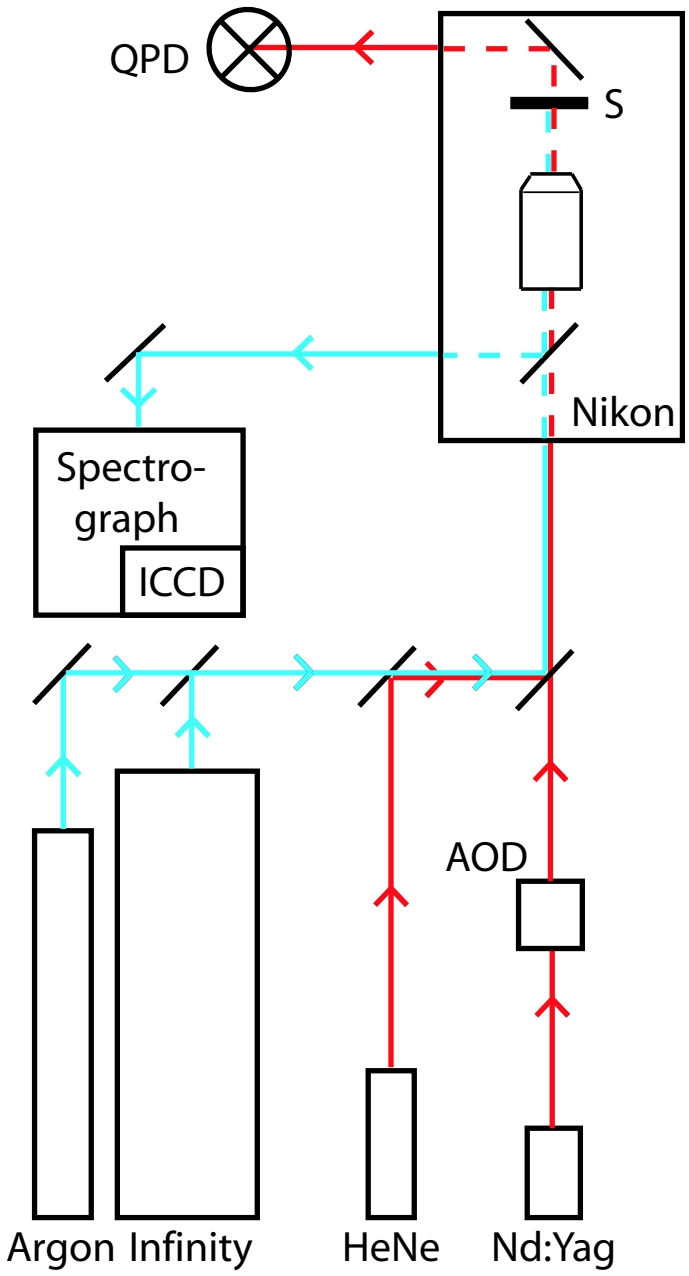

FIG. 3.2: Used setup. The red beam path indicates the optical tweezers components. The blue beam path indicates the part for the excitation of the microspheres and detection of the spectrum. The capillary containing microspheres is indicated by S.

does not heat (and thus deform) the microspheres, nor does it change the refractive index. The beam path of the trapping laser is fully shielded to prevent extra noise in the laser trap due to airflow. The trapping laser light passes through a two axis acousto optical deflector (AOD) of IntraAction Corporation (model number DTD-274HD6). An AOD is a dynamic grating created by passing a sound wave through a Tellurium Dioxide crystal (one crystal for each axis). Both crystals of our double axis deflector

are integrated in one AOD. The AOD deflects the incoming laser beam in several orders of diffraction. By tuning the incident angle on the crystals most of the power (transmission of 40 %) can be passed to the (1,1) order of diffraction. This beam is used to trap the microspheres and can be moved in the focal plane of the microscope by changing the frequency of the sound wave in the crystal [30, 31]. This effectively changes the grating constant and thus the angle at which the beam emerges from the AOD.

After passing through the AOD the beam waist is expanded 4 times to a diameter of 20 mm. The microscope holds a 60x NA 1.2 water immersed objective to focus the laser beam. It has a working distance of 0.18 mm and a transmission of 50 % in infrared. The microsphere is trapped in the laser focus. The infrared light is transmitted through the sample holder and directed to a beam dump.

The second laser in the laser tweezers setup is a 632.8 nm Melles Griot HeNe laser with a maximum continuous wave output power of 15 mW. This laser is used to determine the position of the microsphere. For this purpose a quadrant photo diode (QPD, type Spot 9DMI; UDT) is placed in the back focal plane of the microscope. The QPD consists of a square grid of four Silicon photo diodes. By adding and subtracting the signals of the four quadrants the three dimensional position and movement of the microsphere can be determined [32, 33]. In our experiments the position detection is only done in two dimensions by imaging the trapped microsphere on the QPD. The HeNe overlaps with the infrared Nd:Yag trapping laser and creates an image of the trapped microsphere on the QPD. We do not use the trapping light for position detection because the Silicon photo diodes in the QPD are more sensitive and faster at 632.8 nm. We can reach a detection bandwidth of 100 kHz and an accuracy of about 1 nm/$\sqrt{Hz}$. The accuracy is limited by the background noise level of the electrical circuits in the QPD.

In the next section theory on the optical tweezers is discussed and the method we used to characterize the tweezers is described.

3.3 Characterization of the optical tweezers

Arthur Ashkin pioneered the field of laser-based optical tweezers in the early 1970s. He demonstrated that optical forces could displace and levitate micron-sized particles in different environments [34]. He also showed three dimensional confinement of particles using counter propagating laser beams [35]. The single beam optical tweezers were first demonstrated in 1986 by Ashkin and coworkers [36]. Over the last few years the technique has become mature and is used in many applications in fields like biology, physical chemistry and physics [37].

The content of this section is as follows. First the basic theory of optical tweezers is discussed in section 3.3.1. The emphasis is on the physical understanding of laser trapping and not on the mathematical description. In section 3.3.2 we describe theoretical and experimental considerations regarding the trap stiffness of optical tweezers. The trap stiffness is a factor which determines the quality and stability of the optical tweezers and is therefore an essential parameter in characterizing the trap.

3.3.1 Theory on optical tweezers

Optical tweezers use radiation pressure, a term that refers generally to forces exerted on matter by the absorption, scattering, emission or reradiation of energy (i.e. by photons). Radiation pressure may manifest itself in several ways. Perhaps the most familiar form is the *scattering force*, which is defined as the force due to light scattering that is proportional to the light intensity and acts in the direction of propagation of light. This force can also be regarded as a consequence of the momentum of the scattered photon.

Optical tweezers however owe their trapping ability to the *gradient force*, which is proportional to the spatial gradient in light intensity. It acts in the direction of that gradient. A strong gradient near the focus creates a potential well, in which a particle with a refractive index higher than that of the surrounding medium is trapped in three dimensions. The particle is trapped at the point where the gradient and scattering forces balance. The higher the intensity gradient the better the trap. In order to achieve a high gradient in light intensity an objective lens of high numerical aperture (NA) is used.

The gradient force arises from electric dipoles induced by light which passes through a polarizable medium. The dipoles interact with the electromagnetic field gradient, resulting in a force in the direction of the field gradient. Therefore the gradient force is not only proportional the intensity gradient but also to the polarizability of the trapped object.

When discussing the theory on trapping of particles a discrimination can be made between three different regimes [38]. The Mie theory can be used to calculate the trapping forces for spheres of arbitrary radius and holds in all three regimes. However this calculation is quite complicated. Therefore approximations can be made when distinguishing different regions depending on the sphere size compared to the wavelength of the trapping laser. The geometric regime is applicable when the size of the particle is much bigger than the wavelength ($r \gg \lambda$, section 3.3.1.1). The Rayleigh

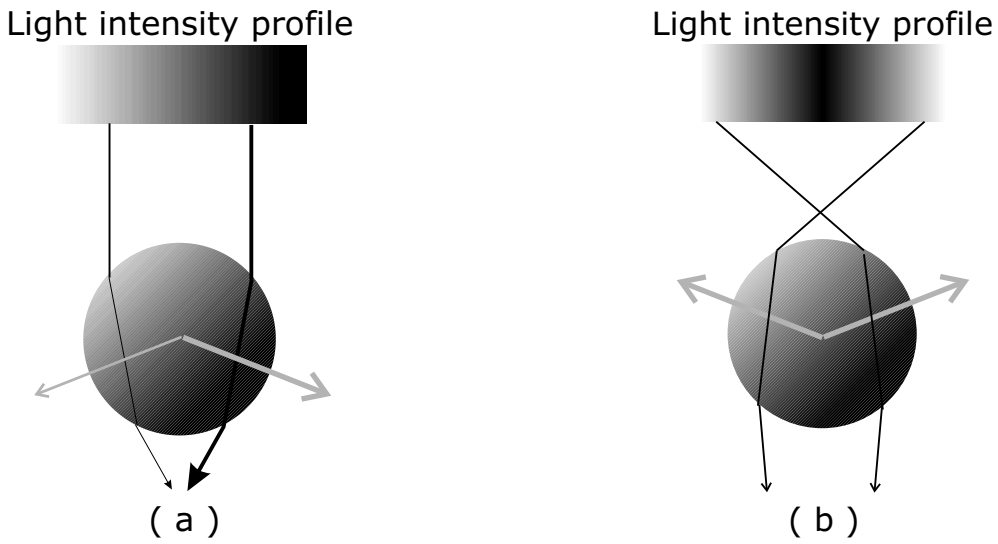

FIG. 3.3: (a) A ray optics picture of the gradient force. A parallel beam of light with a gradient in intensity passes through a sphere with a higher refractive index than it's surrounding. The relative thickness of the two rays indicate the intensity. The rays are refracted and give rise to a force acting through the sphere's center (gray arrows). The brighter ray exerts more force than the dimmer left ray. The sum of all rays tends to pull the sphere toward the brighter (black) region of the beam. (b) Forces in optical tweezers. An incoming beam with an intensity gradient is focussed just before a sphere. The rays are refracted and reaction forces (gray arrows) pull the sphere upward toward the focus. Scattering forces are neglected in this picture.

regime holds for very small particles ($r \ll \lambda$, section 3.3.1.2) and the Mie regime is only used for particles comparable to the wavelength of light($r \sim \lambda$, section 3.3.1.3). Each of these regimes will be discussed shortly in the next subsections.

3.3.1.1 The geometric regime ($r \gg \lambda$)

This geometric regime considers trapped particles which are much larger than the wavelength of the trapping laser. Trapping of particles in this regime can be understood when considering a simple ray-optics picture of the forces [39].

Fig. 3.3 (a) shows the forces playing a role when a spherical particle exhibits a gradient in light intensity. Rays of light carry momentum ($p = h/\lambda$) and are bent by refraction when passing through a dielectric sphere with a refractive index, n, different from the surrounding medium. By conservation of momentum, the rate of change of momentum in the deflected rays conveys an equal and opposite rate of change in momentum to the sphere. The rate of change of momentum produces a force by Newton's second law which is proportional to the light intensity. When the index of refraction of the particle is greater than that of the surrounding medium, the optical force arising from

refraction is in the direction of the intensity gradient. For an index lower than that of the medium, the force is in the opposite direction of the intensity gradient.

When a dielectric sphere is placed in an intensity gradient, the sum of all rays passing through it generates an imbalance in force, tending to push the sphere towards the brighter region of light. Fig. 3.3 (b) shows a sphere in an optical trap. A focus of light acts as a trap because the strong light gradients in its neighborhood all point towards the center. Trapping is stable when the gradient force in the focus is strong enough to overcome the scattering force. If not, the scattering force will project the particle out of the trap's center along the optical axis. As a result of the balance between scattering force and gradient force the axial equilibrium position of the particle is located slightly beyond the focal point. Gravity is not considered in the above description as it has minor influence in experiments.

3.3.1.2 The Rayleigh regime ($r \ll \lambda$)

When the trapped sphere is much smaller than the wavelength of the trapping laser the conditions for Rayleigh scattering are satisfied and optical forces can be calculated by treating the particle as a point dipole. In this approximation the scattering force and the gradient force are dealt with separately.
The scattering force is due to absorption and reradiation of light by the dipole. The force is in the propagation direction of the incident light and is proportional to the intensity of the incident light I_0:

$$F_{scatt} = \frac{a^6}{\lambda^4}\frac{(m^2-1)}{(m^2+2)}\frac{n_m I_0}{c}$$

where a is the radius of the trapped particle, λ is the wavelength of the trapping laser, m is the contrast in index of refraction, n_m is the index of refraction of the medium, c is the speed of light in vacuum . The gradient force arises from the interaction of the induced dipole with the intensity gradient of the incident field:

$$F_{grad} = \frac{n_m a^3}{c}\frac{(m^2-1)}{(m^2+2)} \bigtriangledown I_0$$

The gradient force is proportional to the intensity gradient of the incident field I_0 and points in the positive gradient direction.

3.3.1.3 The Mie regime ($r \sim \lambda$)

The Mie regime is applicable to all situations because it describes the scattering of an electromagnetic wave by a sphere of arbitrary radius. In practice Mie theory is only used when the size of the particle is comparable to the wavelength of light ($0.1\lambda < r < 10\lambda$) because in the Rayleigh and geometric regime approximations can be

made which simplify the calculations. In the Mie regime the force on the particles can not be calculated using the dipole approximation. In this case the Maxwell equations have to be solved and the force can be calculated from this solution [40, 41]. A good approximation to the solution is to generalize the Mie theory. Mie scattering theory describes the scattering of a plane wave by a particle of arbitrary size. If the plane wave is substituted by a Gaussian beam profile a good approximation can be obtained for the electric fields inside and outside the particle for an incoming focussed beam.

Most of the trapping experiments take place in the Mie regime. As explained above it is hard to calculate the scattering and gradient forces when the size of the particle is comparable to the wavelength. There are however experimental methods which can help to determine the quality and stability of the trap (see for example [38]). One of these methods will be discussed in the next paragraph.

3.3.2 Trap stiffness

An experimental method can be used to characterize the trap. This is more accurate than a theoretical calculation because we do not exactly know the Gaussian beam shape of the trapping laser and the transmission properties of the objective. The method used in this experiment is based on the determination of the power spectrum of the Brownian motion of a trapped microsphere [42]. Brownian motion is caused by thermal fluctuations in the fluid. It causes the particle to move in a random way due to collisions with other molecules in the fluid. By trapping the particle and increasing the power of the trapping laser the Brownian motion of the particle will be suppressed by the gradient force. By measuring the power spectrum of the Brownian motion of the trapped particle the trap stiffness (in units of force) can be calculated. First the theory regarding the trap stiffness measurement is discussed in section 3.3.2.1 followed by section 3.3.2.2 discussing the method used to determine the trap stiffness experimentally.

3.3.2.1 Theory of trap stiffness measurements

Consider the one dimensional equation of motion for a particle undergoing Brownian motion in a viscous fluid while confined to a harmonic potential well:

$$m_p\ddot{x} + \gamma\dot{x} + \kappa_x x - F_{rand}(t) = 0 \tag{3.1}$$

where m_p is the mass of the particle, γ is the viscous drag coefficient (defined by $\gamma = 6\pi\eta a$ with η the viscosity of the fluid), κ_x is the trap stiffness and F_{rand} represents the random fluctuating force exerted on the trapped particle due to collisions with molecules in the surrounding fluid. Equation (3.1) is also referred to as the Langevin equation.

This equation can be simplified by acknowledging that a small particle trapped in water behaves as an overdamped oscillator: the viscous drag term will dominate the inertial term involving the mass of the particle. Assuming that $F_{rand}(t)$ has a time-average of zero and taking the fourier transform of the simplified equation (3.1) we get:

$$(\kappa_x - i2\pi f\gamma)X(f) = F_{rand}(f) \tag{3.2}$$

Taking the square modulus of both sides of equation (3.2) gives us:

$$|X(f)|^2 = \frac{|F_{rand}(f)|^2}{4\pi^2\gamma^2(f_c^2 + f^2)} \tag{3.3}$$

where f_c is the corner frequency:

$$f_c = \frac{\kappa_x}{2\pi\gamma} \tag{3.4}$$

The quantity $|X(f)|^2$ is the two-sided power spectrum of the random Brownian motion of the particle. The value can be interpreted as the contribution to the total variance made by a signal with frequency f.

In experiments the distinction between positive and negative frequencies is not necessary, therefore we assume that $|X(f)|^2 = |X(-f)|^2$. In this case we can use the power spectral density (or one-sided power spectrum), defined as:

$$S_x(f) \equiv |X(f)|^2 + |X(-f)|^2 = 2|X(f)|^2, \text{ for } 0 \leq f \leq \infty \tag{3.5}$$

In equation (3.3) the time average of F_{rand} is given by [43]:

$$|F_{rand}|^2 = 2\gamma\kappa_b T \tag{3.6}$$

With equation (3.5) this gives us for the power spectral density of the random motion of a colloidal particle in a fluid:

$$S_x(f) = \frac{k_b T}{\gamma\pi^2(f_c^2 + f^2)} \tag{3.7}$$

Equation (3.7) can be used to determine the trap stiffness. How this is done in practice is discussed in the next section.

3.3.2.2 Trap stiffness measurements using a quadrant photo diode

In order to measure the trap stiffness we have to measure the power spectral density (PSD) of the system (equation (3.7)). This can be done using a quadrant photo diode (QPD). A QPD is an array of four detectors in a square grid. The QPD is placed in

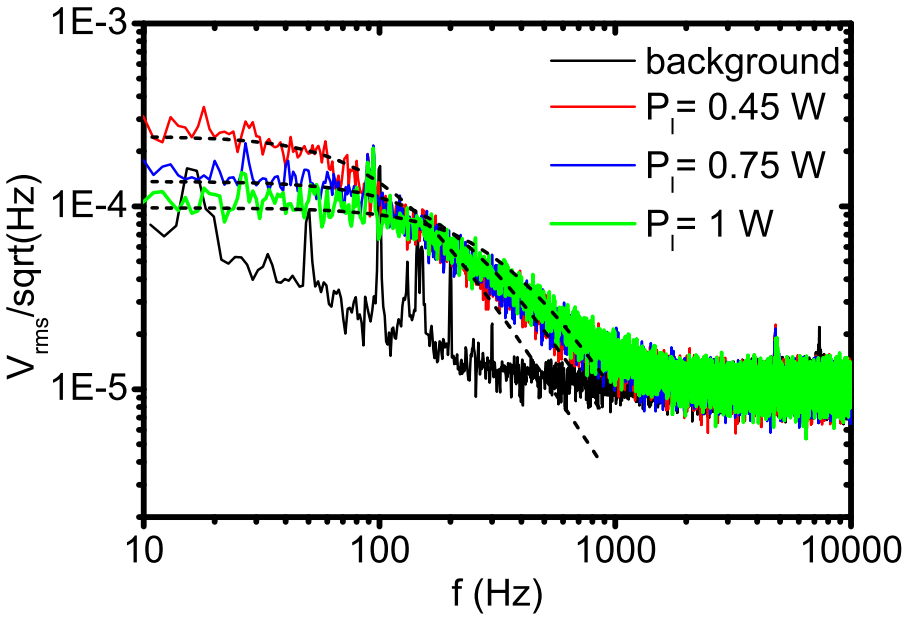

FIG. 3.4: Power spectral density for lateral motion of the microsphere. The black line indicates the PSD of the background signal (trapping laser on and no microsphere trapped). The green, blue and red line indicate the PSD of the Brownian motion of the trapped particle, recorded with different trapping powers, respectively 0.45 W, 0.75 W and 1 W. The dashed curves indicate the theoretical PSD for trap stiffnesses of 66 $\frac{pN}{\mu m}$, 120 $\frac{pN}{\mu m}$ and 190 $\frac{pN}{\mu m}$ respectively.

the back focal plane of the microscope with the trapped particle imaged in the center of the detector. A HeNe laser emitting at 632.8 nm is used to image the particle on the QPD. Brownian motion of the microsphere is detected as a change in signal in each of the four quadrants. By fourier transforming the time resolved signal on the QPD the PSD for the Brownian motion of the microsphere in the lateral and axial direction can be determined [32, 33].

The signal detected by the QPD is subject to different sources of noise [44]. The total amount of noise can be divided into two main categories, instrumental and thermal noise. Instrumental noise can have a large number of sources like stability of the laser (trapping laser and HeNe), vibration of a mirror or airflow through the beam path. Instrumental noise is mainly low frequency noise. Thermal noise has its origin in the Brownian motion of the trapped particle and is very broad in frequency. It is the latter contribution to the total noise we ar interested in because the amount of suppression of the Brownian motion characterizes the trap stiffness of the optical tweezers.

The axial and lateral PSD of the Brownian motion were recorded under two different

$\mathbf{P_{trap}}(W)$	$\mathbf{f_c}(Hz)$	$\kappa_\mathbf{x}(\frac{\mathbf{pN}}{\mu\mathbf{m}})$
0.45	112	66
0.75	211	120
1.00	328	190

Table 3.2: Trap stiffness κ_x for a 10.1 μm microsphere in water for several trapping laser powers P_{trap}. Trap stiffness is calculated using equation (3.4) and the cut-off frequency f_c as determined from the PSD fits shown in Fig. 3.4.

conditions. Fig. 3.4 shows the PSD for lateral movement of the microsphere in the optical tweezers. The first spectrum (black line) is recorded with the trapping laser on and no microsphere trapped in the optical tweezers. The noise recorded here represents 1/f noise. This noise originates from the instability of the laser and the optical components in the setup. The trapping laser beam is fully shielded as it travels through air to minimize the airflow through the beam path.

The other PSD of the noise in the trap are recorded with a 10.1 μm diameter microsphere (as described in section 3.1) trapped by the optical tweezers. The trapping laser power is varied from 0.45 W to 1 W as indicated in Fig. 3.4. The value given is the real laser power on the sample. As can be seen from the figure the plateau value in the PSD of the Brownian motion of the microsphere decreases as the trapping power increases. This indicates more suppression of low frequency motion of the microsphere in the trap as the laser power increases. Also the cut-off frequency increases with trapping power. The cut-off frequency is determined by fitting the solution to the Langevin equation (3.7) to the experimental data. Equation (3.4) can be used to determine the trap stiffness. The results are shown in table 3.2. The error in the trap stiffness is quite large because the fit of equation (3.7) to the experimental data is not perfect. We estimate the error in the trap stiffness to be about 25 %.

As expected the trap stiffness increases as the trapping laser power increases. Generally the trap stiffness in both lateral directions (x and y) is comparable as the intensity gradient of the trapping laser is symmetrical (this depends on the beam profile and alignment of the objective though). In the axial direction, however, the intensity gradient of the trapping laser is lower. This results in a lower trap stiffness compared to the lateral direction. In our case the axial trap stiffness is still good enough to be able to lift the 10.1 μ m diameter microspheres from the surface.

Chapter 4

Experimental results

We experimentally studied resonances in the emission spectrum of dye doped polystyrene microspheres. The resonances in the spectrum are the result of the natural modes of the microsphere. The location of the morphology dependent resonances (MDRs) depends on the size of the sphere and the refractive index of the sphere and the medium, as is explained in chapter 2.1. In the experiments, we focus on the resonances occurring at the peak of the emission spectrum of the dye around 515 nm (Fig. 3.1). At these resonances the dye in the microsphere has the highest gain and therefore from a physical point of view, these resonances are most interesting. When the pump power is high enough, the cavity loss rate can be overcome by the gain. In this case the resonance becomes a laser resonance.

Two series of experiments have been performed. First the microspheres were excited using continuous wave (CW) excitation (section 4.1). We performed a series of measurements in which the refractive index of the environment was tuned. An increase in refractive index of the medium decreases the contrast in index of refraction and changes the linewidth and frequency of the resonances. The full width at half maximum of the resonances and the TE-TM mode spacing were measured and compared to theoretical values.

The second series of measurements was done using pulsed laser excitation (section 4.2). The pulsed excitation laser has a much higher peak excitation power than the CW excitation. We measured emission spectra of a microsphere as a function of pump power. At a pump power above threshold multi-mode lasing was observed in the emission spectrum. The output power of a laser line shows a clear lasing threshold. The gain in the microsphere is calculated using the theory described in section 2.3.

As discussed in chapter 2 the Mie scattering cross sections can not be directly compared to this experiment due to some conceptual differences. Therefore we adopted a model developed by Chew and coworkers [16] which describes the fluorescence from dipoles

embedded in spherical particles (section 2.3). This model enables a direct comparison between experiment and theory. All theoretical fits shown in this chapter are fits calculated from the dipole emission model as described in equation (2.25). Section 2.1 concluded that the Mie theory and the fluorescence model are not valid when the system is in a lasing condition. We do not, at present, have a model which describes the full system above the threshold. Therefore the spectra are not fitted with theoretical curves when the pump power is above threshold.

4.1 Continuous wave excitation

In order to examine the emission spectra of a 10.1 μm dye doped polystyrene microsphere we trapped a single microsphere with the optical tweezers as described in section 3.3. In order to prevent interaction with the glass surface of the sample holder the microsphere is lifted a distance of several times its diameter from the surface. This is done by moving the focus of the infrared trapping laser away from the glass surface into the capillary. The power of the trapping laser is about 30 kW/mm^2 in the focus with a focal size of 1.5 μm (full width at half maximum). The dye is excited with a continuous wave Argon laser at 488 nm. The excitation power is 0.5 mW, measured on the sample. The scattering force from the infrared trapping pushes the microsphere out of the laser focus. Therefore the microsphere is not trapped in the focus but slightly further from the objective so the whole microsphere is illuminated by the Argon laser light.

The resonances in the measured spectrum have been identified by fitting the spectrum to theoretical spectra (section 4.1.2). In section 4.1.3 we present the method we used to measure the full width at half maximum of the resonances and the TE-TM mode spacing. In section 4.1.4 we show the results of the experiments in which we tuned the refractive index of the surrounding medium. The experimental results are compared to the theory.

4.1.1 Measured spectrum

The emission spectrum we obtained from a single dye doped polystyrene microsphere immersed in water is shown in Fig. 4.1. Sharp resonances are observed in the spectrum due to MDRs inside the sphere [14]. The spectrum is an average over 10 measurements with an integration time of 0.5 s per measurement. The mode numbers are indicated in the figure. The dashed line shows a theoretical curve with fit parameters $m_0 = 1.335$ (fixed value), $m_I = 1.586$ and $a = 5.33$ μm (fitting parameters). These values are well within the limits of the variations given in section 3.1. The theoretical spectrum is convolved with a Gaussian of width 0.13 nm to compensate for the response function of the spectrograph. The Gaussian width of this response function is determined

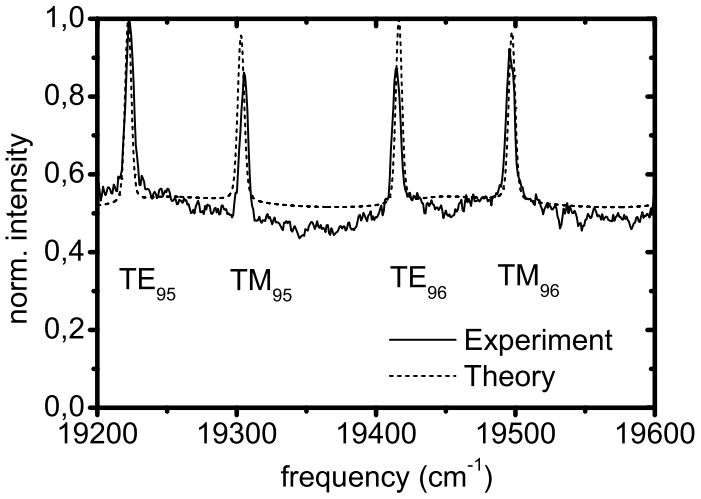

FIG. 4.1: Emission spectrum of a single dye doped polystyrene microsphere immersed in water pumped with 0.5 mW of CW light. The spectrum is an average over 10 measurements with an integration time of 0.5 s per measurement. The dashed line shows a theoretical curve with parameters $m_0 = 1.335$ (fixed value), $m_I = 1.586$ and $a = 5.33$ μm (fitting parameters). Both theory and experiment are normalized to the peak value. The experimental spectrum is corrected for a background due to stray light.

from the width of a HeNe laser line recorded by the spectrograph. Both theory and experiment are normalized to the peak value and the experimental result is corrected for a background intensity due to stray light entering the spectrograph.

Note that every microsphere used in the experiments has different resonant frequencies. This is caused by a small variation in the size a of the microspheres.

4.1.2 Mode identification

The mode numbers shown in Fig. 4.1 are identified by examining the denominators D_n (TM polarization) and D'_n (TE polarization) in equation (2.24). These denominators appear in the expressions for the radiation rate (equations (2.22) and (2.23)). Because D_n and D'_n appear as denominators in the expressions for the scattered and emitted fields we refer to the complex zeros $\omega = \omega_R + i\Gamma$ of D_n and D'_n as poles. These are the eigenfrequencies of the sphere. Each eigenfrequency corresponds to a certain mode number n, which can be identified by fitting a theoretical emission spectrum to the measured emission spectrum.

Fitting a theoretical curve to the measured emission spectrum is done by fixing m_0

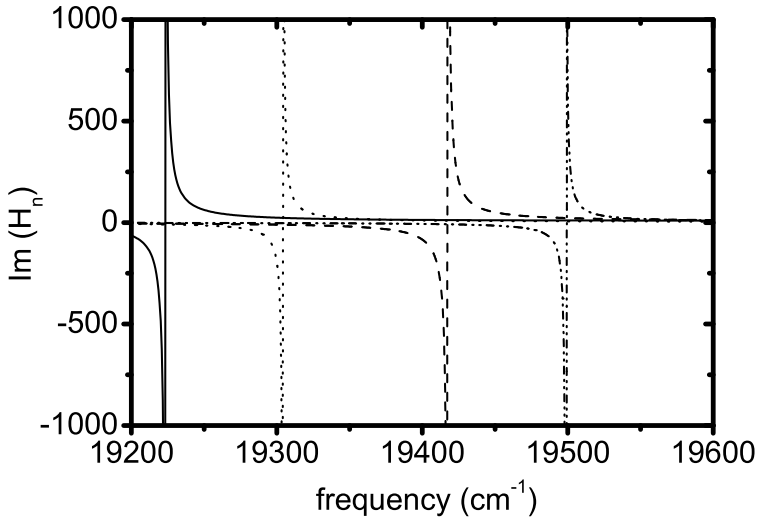

FIG. 4.2: The imaginary part of D_n^{-1} and $D_n'^{-1}$ plotted versus wavenumber for mode numbers 95 and 96. The figure shows $D_{95}'^{-1}$ (solid), D_{95}^{-1} (dot), $D_{96}'^{-1}$ (dash) and D_{96}^{-1} (dot-dash). The vertical axis is truncated at 1000.

to 1.3325. The variables a and m_I are obtained by overlapping the resonances in the theoretical emission spectrum to the measured resonance frequencies.

By plotting D_n and D_n' for the variables m_0, m_I and a obtained by the fitting procedure, the mode numbers n of the resonances can be identified. Fig. 4.2 shows the imaginary part of D_n^{-1} and $D_n'^{-1}$ plotted versus wavenumber for mode numbers 95 and 96.

4.1.3 Experimental and theoretical determination of the full width at half maximum and the TE-TM mode spacing

The experimental full width at half maximum and mode spacing of neighboring TE and TM resonances can be determined by fitting a model lineshape to each individual resonance in the measured emission spectrum. The lineshape function we fit to the individual resonances is a Voigt profile [45] with a second order background correction. A Voigt function is the convolution of a Lorentzian and a Gaussian profile. The background correction is added because the fluorescent background of the experimental spectrum is not flat. If we leave out the background correction, we find the fit parameters are influenced by the background. The Voigt lineshape models the Lorentzian width of the resonance as measured through the Gaussian response

fraction water	***nD (293K)***	***nD (298K)***
1.0	1.3332	1.3325
0.8	1.3554	1.3544
0.6	1.3760	1.3751
0.4	1.3992	1.3978
0.2	1.4148	1.4131
0.0	1.4317	1.4302

Table 4.1: Refractive indices of mixtures of water with ethylene-glycol measured at 589 nm. The refractive indices were measured at a temperature of 293 and 298 K and are shown as a function of the volume fraction of water.

function of the spectrograph. The model function is given by:

$$y(f) = y_0 + Af + Bf^2 + C\frac{2\ln 2}{\pi^{3/2}}\frac{w_L}{w_G}\int_{-\infty}^{\infty}\frac{e^{-t^2}}{\left(\sqrt{\ln 2}\frac{w_L}{w_G}\right)^2 + \left(\sqrt{4\ln 2}\frac{f-f_c}{w_G} - t\right)^2}dt \quad (4.1)$$

where y_0 is the offset, A and B are constants for the background correction, C is the amplitude, w_G is the (fixed) Gaussian width, w_L is the Lorentzian width, f is frequency and f_c is the center frequency of the resonance. The Lorentzian width determines the width of the resonance in the microsphere and the Gaussian width (0.13 nm) corrects for the response function of the spectrograph. The FWHM of the resonances is equal to w_L. The mode spacing is the difference of the two values of f_c for the two fits of the TE_{96} and TM_{96} mode.

The theoretical values for the full width at half maximum and TE-TM mode spacing are found from the complex poles x_0, which are zeros of D_n and D'_n. As mentioned in section 2.3 the resonant behavior of the Mie scattering theory and the fluorescence model is the same. The real part of x_0 corresponds to the frequency of the resonance while the imaginary part gives the width of the resonance as in equation (2.16).

4.1.4 Tuning the refractive index of the medium

In the experiments we tuned the refractive index of the surrounding medium m_0. The refractive indices we used are shown in table 4.1. Table 4.1 shows the volume fractions of water and ethylene-glycol used and the refractive index measured at both 293 and 298 K. The refractive indices are measured at 589 nm while the spectra are measured around 515 nm. As the dispersion of water is small over this wavelength range [29] the change in refractive index of the mixtures is assumed to be less than 0.005.

Emission spectra were measured for all values of m_0 listed in table 4.1 (environmental

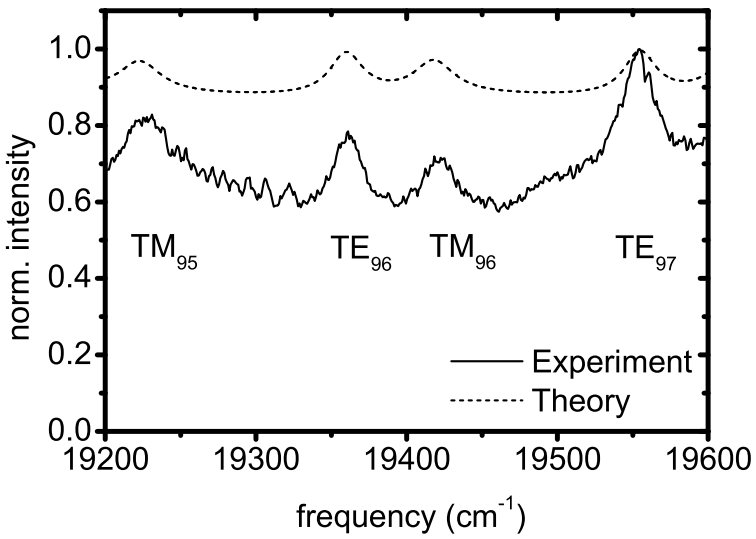

FIG. 4.3: Spectrum of a single dye doped polystyrene microsphere immersed in a mixture of water and ethylene glycol ($m_0 = 1.3978$). The spectrum is an average over 20 measurements with an integration time of 0.05 s per measurement and is background corrected. The dashed line shows a theoretical curve with parameters $m_0 = 1.3978$ (fixed value), $m_I = 1.586$ and $a = 5.319$ μm (fitting parameters). Both theory and experiment are normalized to the peak value.

temperature 298 K). The measurement with $m_0 = 1.4317$ (pure ethylene glycol) did not show any resonances because the resonance quality factor was very low due to the low refractive index contrast ($\frac{m_I}{m_0} = 1.11$). It was impossible to distinguish the resonances from the fluorescent background. Therefore data of this measurement is not included in the figures.

Fig. 4.3 shows the measured emission spectrum for a refractive index in the medium of $m_0 = 1.3978$. The spectrum is an average over 20 measurements with an integration time of 0.05 s per measurement. The mode numbers are indicated in the figure and determined using the method described in section 4.1.2. The emission spectrum is normalized to the peak value and background corrected. The dashed line shows a theoretical fit with parameters $m_0 = 1.3978$ (fixed value), $m_I = 1.586$ and a=5.319 μm (fitting parameters).

As can be seen the mode spacing is smaller compared to the mode spacing in the microspheres immersed in water (Fig. 4.1). The TE-TM mode spacing is a result of the phase shift for total internal reflection. The phase shift of one total internal reflection is different for TE and TM polarization and depends on the refractive index contrast [46]. By tuning m_0 we change the refractive index contrast and the phase

shift between TE and TM polarized modes. This results in a different TE-TM mode spacing for different refractive index contrast.

Also the resonances are much broader for the lower refractive index contrasts. A change in refractive index contrast changes the microsphere resonance quality factor: the higher the index contrast the higher the microsphere resonance quality factor. As the resonance quality factor is directly related to the linewidth of a mode ($Q = \frac{\omega}{\Delta\omega}$) a change in index contrast results in a change in linewidth.

The signal to noise ratio in Fig. 4.3 is approximately a factor 2 lower than in the measurement in pure water ($m_0 = 1.3325$). The is because the spectral intensity of the dye emission in the resonances is a factor of 20 lower. The low intensity in the resonances causes the fluorescent background to be dominant in the spectrum and makes it hard to compare the theoretical to the experimental spectrum. This is in general the case for low refractive index contrasts because the resonances in the emission spectrum are low in intensity and broad. As can be seen in Fig. 4.3 the peak positions still compare very well to the theory.

Considering the emission spectra measured at five different refractive index contrasts the full width at half maximum and TE-TM mode spacing can be compared to theoretical values. In order to do so the experimental TE_{96} and TM_{96} resonances are fitted with a Voigt profile as described in section 4.1.3. Our results are shown in the next two sections. First the full width at half maximum is examined (section 4.1.4.1) followed by the TE-TM mode spacing (section 4.1.4.2).

4.1.4.1 Full width at half maximum

Fig. 4.4 shows the full width at half maximum as function of m_0 for the (a) TE_{96} and (b) TM_{96} mode. The width shown is the Lorentzian width of a Voigt profile (equation (4.1)). The size of the error bars is taken from the error in the Lorentzian width of the fits. The measurement in pure water ($m_0 = 1.3325$) has a larger error bar in the negative direction because the measured Lorentzian width is very small compared to the Gaussian width of the response function of the spectrograph. It is very well possible that the Lorentzian width is much narrower than we can measure with the spectrograph. The theoretical curve (dashed line) is calculated for a microsphere of refractive index $m_I = 1.586$ and radius $a = 5.3$ μm using the method described in section 4.1.3.

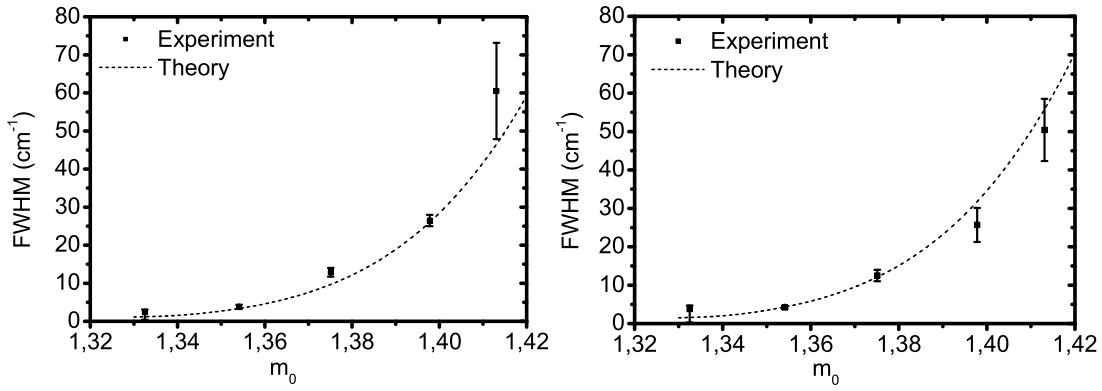

FIG. 4.4: Full width at half maximum as function of m_0 for the (a) TE_{96} and (b) TM_{96} mode. The widths are the pure Lorentzian widths from a fit with a Voigt profile. The error bars are the fitting errors in the Lorentzian width. The dashed line shows the theoretical full width at half maximum for a sphere with radius $a = 5.3$ μm and $m_I = 1.586$.

We can calculate the resonance quality factor from the measured widths of the resonances. For a polystyrene microsphere immersed in water we find a resonance quality factor of $8 \cdot 10^3 \pm 2 \cdot 10^3$ for the TE_{96} mode and $5 \cdot 10^3 \pm 2 \cdot 10^3$ for the TM_{96}. The contrast in index of refraction is 1.195 in this measurement. Decreasing the contrast in index of refraction to 1.137 ($m_0 = 1.3978$) results in a decrease in resonance quality factor to 750 ± 100 for both the TE_{96} and TM_{96} modes.

4.1.4.2 Mode spacing

Fig. 4.5 shows the mode spacing between the TE_{96} and TM_{96} modes as a function of refractive index m_0. Measurements were performed on samples with m_0 as stated in table 4.1. The mode spacing is measured by fitting the resonances with a Voigt profile (equation (4.1)) and subtracting the central frequencies of the TE and TM resonance. The error bars result from the fitting errors in f_c. The dashed curve shows the theoretical result for a sphere with $m_I = 1.586$ and $a = 5.3$ μm. The theoretical mode spacing is calculated from the real part of the poles of D_n and D'_n. It is seen from Fig. 4.5 that the mode spacing decreases with m_0 and that this is well described by the theoretical curve.

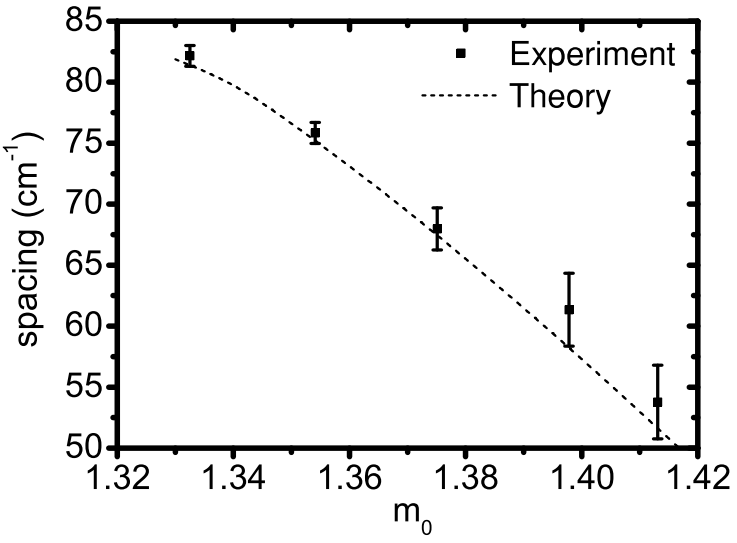

FIG. 4.5: Mode spacing between modes TE_{96} and TM_{96} as a function of refractive index of the medium m_0. The error bars result from the fitting error in f_c in equation (4.1). The dashed line shows the theoretical curve for a sphere of refractive index m_I=1.586 and radius $a = 5.3$ μm.

4.2 Pulsed laser light excitation

This section describes the measurements we performed on single dye doped polystyrene microspheres using pulsed laser light excitation. The most important difference with the CW laser excitation is the peak power, which is a factor of 10^5 higher for pulsed laser excitation. A single microsphere is trapped with optical tweezers and lifted from the glass surface of the capillary. The microsphere is immersed in water, which has a refractive index of $m_0 = 1.3325$ (see table 3.1, environmental temperature 298 K). The power of the trapping laser is about 30 kW/mm^2 in the focus with a focal size of 1.5 μm (full width at half maximum). The excitation laser focus is about 6 μm. As the microsphere is not trapped in the focus due to scattering forces the excitation laser illuminates the whole sphere. The excitation light source is a pulsed Coherent Infinity-XPO emitting at 470 nm with a repetition rate of 50 Hz and a pulse duration of ~ 3 ns. Considering the repetition rate and pulse duration the peak power is a factor 10^8 higher than the average power.

The gain in the microsphere is provided by the population inversion in the dye embedded in the polymer matrix and depends on the power and frequency of the excitation laser. The gain spectrum has approximately the shape of the excitation spectrum shown in Fig. 3.1. The lasing resonances become laser lines when the excitation is powerful enough to create sufficient gain in the microsphere (provided by population inversion in the dye). At the threshold pumping power the gain compensates for the loss and the natural mode of the microsphere is a laser line. Pulsed laser excitation provides enough pump power to cross the laser threshold and observe (one or more) laser lines in the emission spectrum.

4.2.1 Lasing threshold

When excited above threshold, the microsphere will exhibit one or more laser lines. The number of laser lines strongly depends on the sphere size, sphericity and surface roughness of the microsphere and can not be predicted on forehand. Other factors which influence the number of laser lines in a microsphere are the quantum efficiency and the gain spectrum of the dye. Smaller spheres have a larger free spectral range and therefore have less natural modes at frequencies in the gain spectrum of the dye.

In order to measure the lasing threshold in the microspheres the emission spectrum is measured as a function of pump power on the sample. Fig. 4.6 (a) shows the emission spectrum for low pumping power (0.05 μW average power on the sample). The emission spectrum is an average over 10 frames with an integration time of 10 s per frame and is corrected for background due to stray light. The spectrum is fitted with a theoretical spectrum (dashed line) as in equation (2.25). Using the same procedure as described in

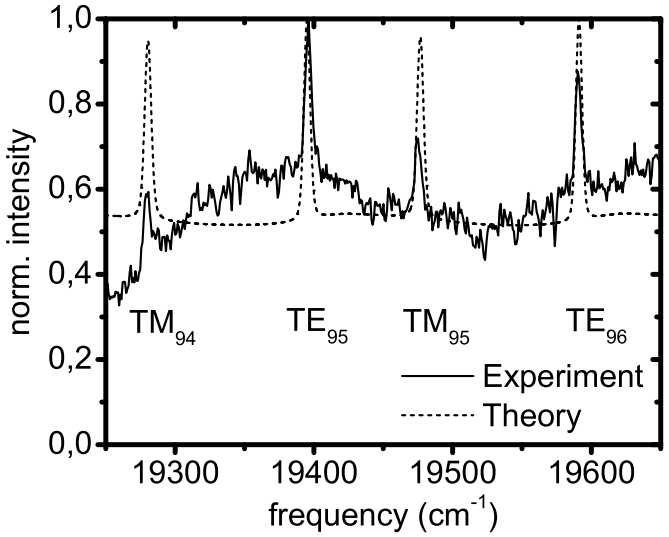

(a)

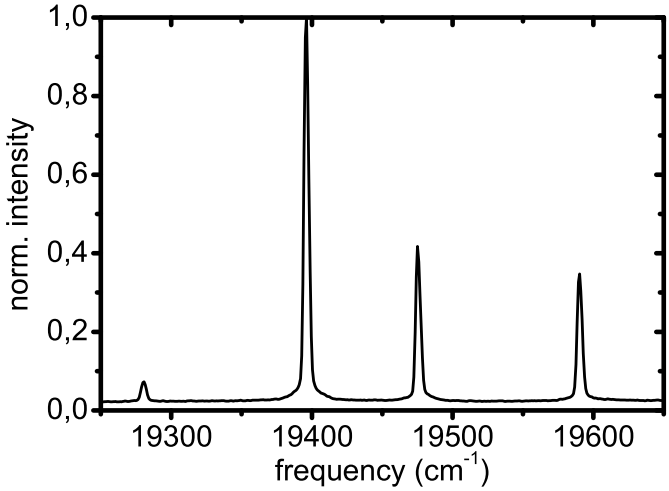

(b)

FIG. 4.6: (a) Spectrum of a microsphere excited with a low pump power (0.05 μW average power on the sample). The mode numbers are identified and shown in the figure. The spectrum is an average over 20 frames with an integration time of 10 s per frame and is corrected for background due to stray light. The dashed line shows a theoretical fit for a microsphere with $a = 5.29$ μm (fixed value), $m_0 = 1.3325$ and $m_I = 1.583$ (fitting parameters). (b) Spectrum of the same sphere measured at high pump power (5 μW average power on the sample). The spectrum is an average over 20 spectra with an integration time of 0.5 s per spectrum and is background corrected.

section 4.1.2 we find a fit with sphere radius $a = 5.29$ μm. The refractive indices have a value of $m_0 = 1.3325$ (fixed value) and $m_I = 1.583$ in the theoretical curve. These

values are well within the limit of the variations as stated in section 3.1. The emission spectrum resembles the CW excitation spectra shown in Fig. 4.1. The resonances have approximately the same frequency, this only differs due to the size dispersion in the batch of microspheres. The signal to noise ratio is about a factor of 3 lower though because the average excitation power is a factor of 10^4 lower than in the CW excitation measurements.

Fig. 4.6 (b) shows the emission spectrum of the same microsphere but now we increased the pulse energy so that the average pump power is 5 μW on the sample instead of 0.05 μW. The pulsed laser power on the sample now corresponds to a peak excitation power of 33 Watt considering the pulse duration of 3 ns and the repetition rate of 50 Hz. The emission spectrum is an average over 20 spectra with an integration time of 0.5 s per spectrum. Three lasing modes are visible in the spectrum (TE_{95}, TM_{95} and TE_{96}). In many emission spectra we measured, lasing was seen in this multi-mode fashion. We also observed single mode lasing. Generally lasing was more often observed in TE modes than TM modes. Single mode lasing was always observed in the TE_{95} mode. As mentioned in chapter 2, TE polarized modes are narrower than TM modes. A narrower resonance implies a lower loss factor in the cavity which explains why we observe lasing more often in TE modes than in TM modes.

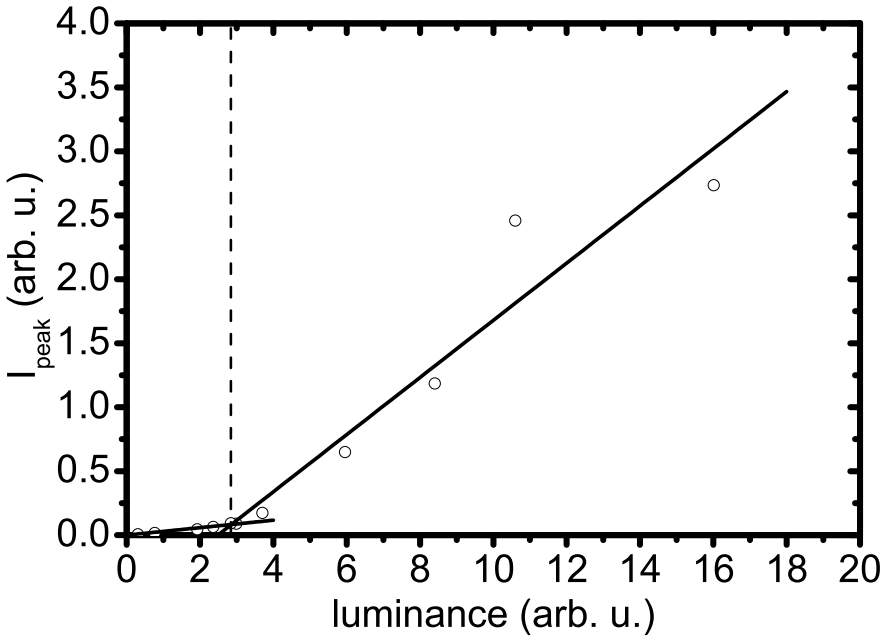

FIG. 4.7: Evolution of the peak intensity in the TE_{95} lasing mode at 19400 cm^{-1} as a function of luminance.

At pump powers above threshold the intensity of the laser mode is up to 30 times the intensity of the fluorescent background. To verify the mode is in a lasing condition the emitted power in the lasing mode versus the absorbed pump power should be considered. This relation is shown in Fig. 4.7. We could not accurately measure the (very low) absorbed pump power in the microsphere. Therefore an alternative measure of the absorbed power, the luminance, is placed on the x-axis of the threshold graph. The luminance is the total integrated intensity in the emission spectrum and is assumed to be proportional to the absorbed pump power by the microsphere. This allows us to see the lasing threshold without the need to measure the absorbed pump power. We do not obtain a quantitative measure for the lasing threshold but we do see the expected threshold behavior [47]. The absolute lasing threshold will be different for every microsphere because it depends on the resonance quality factor of the lasing mode.

4.2.2 Measurement of the gain in the microsphere

In section 2.1 we concluded that the width of a certain mode will change from a positive to a negative value if there is gain present in the cavity. The solution to the Mie theory is non physical for modes with a negative width. However we can say that the mode numbers having a zero or negative width are lasing modes in the spherical particle: Increasing the gain decreases the width of the resonance (or: increases the resonance quality factor). Eventually the width of the resonance passes zero and becomes negative. When a mode has a zero width the quality factor for this mode is infinity and the mode is a lasing mode.

In the theory we considered a constant gain. However, in the experiments we performed, the gain saturates when the pump power increases to values above threshold. Increasing the pump power further does not affect the gain in the microsphere anymore. This is called gain saturation and is a well known effect (see for example [47]).

Fig. 4.8 shows the theoretical width of the TE_{95} and TM_{95} modes in a polystyrene microsphere ($m_I = 1.586$) of radius 5.29 μm immersed in water ($m_0 = 1.3325$). The width of the modes is plotted as a function of the imaginary part of m_I, the gain in the microsphere. At a certain value for the gain in the microsphere the width of the mode crosses zero and becomes negative. The point at which the width is zero is the lasing threshold of the mode. As expected the TE mode has a lower threshold than the TM mode because it is narrower in frequency.

From Fig. 4.8 the gain inside the particle can be determined for the experimental lasing modes TE_{95} and TM_{95}. As we saw in the measured emission spectrum both the TE_{95} and TM_{95} modes are laser modes (Fig. 4.6 (b)). For both modes we can

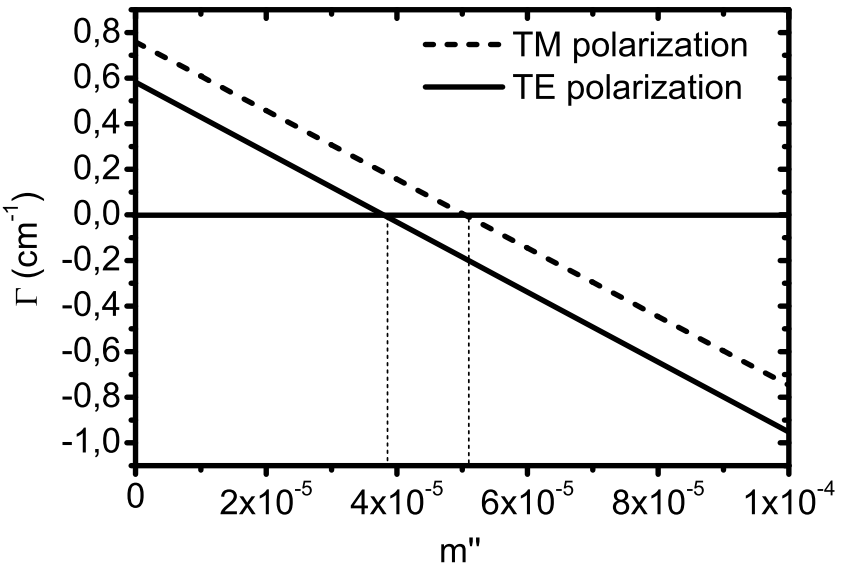

FIG. 4.8: Width of the TE_{95} and TM_{95} resonances as a function of the imaginary part of the refractive index m_I of the microsphere. The refractive index of the medium m_0 is 1.3325 (water). The sphere radius is set at 5.29 μm with the real part of m_I being 1.586.

determine the gain in the refractive index from Fig. 4.8. Due to gain saturation this is the gain at threshold as well as above threshold pump power. The gain for the TE_{95} mode corresponds to $\mathrm{Im}(m_I) = 3.9{\cdot}10^{-5}$ when the mode is in a lasing condition. The TM_{95} mode needs a higher gain in order to pass the threshold because it has a higher loss factor. At and above threshold it has a gain of $\mathrm{Im}(m_I) = 5.1{\cdot}10^{-5}$.

Chapter 5

Conclusions and recommendations for further research

5.1 Conclusions and discussion

In this thesis the lasing resonances in dye doped polystyrene microspheres were studied. The results were compared to Mie scattering theory and a model describing the emission of dipoles in a spherical cavity [16, 17].

We extended the classical Mie scattering theory to refractive indices with gain (positive imaginary part). This extension was found to be invalid for sizeparameters exceeding a critical value. When increasing the sizeparameter beyond the critical sizeparameter, the linewidth of a mode eventually crosses zero and becomes negative. The region where the mode has a negative linewidth is not a physical solution to the Mie scattering problem. Effectively a linewidth of zero implies an infinite resonance quality factor. We found that the combination of cavity size and gain in the refractive index at which the linewidth of the mode number crosses zero, is the lasing threshold for this resonance. The extension of the Mie scattering theory is therefore only valid in regions below the lasing threshold. In order to gain more insight in the point at which the extension of the Mie theory fails, we considered a Fabry Perot cavity with a gain medium between the mirrors. We found that, for a certain amount of gain in the medium, the solution for the cavity transmission is invalid beyond a critical cavity size, which is consistent with our conclusion regarding the extension of the Mie theory.

We measured the emission spectrum of the dye embedded in the microsphere using low power continuous wave excitation. The emission spectra showed modes at frequencies corresponding to morphology dependent resonances. We identified the mode numbers of the resonances in the emission spectrum of the dye by fitting the experimental spectrum with a theoretical spectrum. Alternating TE and TM modes were observed

with mode numbers around 95. The theoretical spectrum was obtained from the fluorescence of dipoles in a spherical cavity and showed excellent agreement with the experimental emission spectrum. The background as well as the peak height are of the same order.

We measured the full width at half maximum and TE-TM mode spacing of the observed resonances as a function of the refractive index of the environment. We found that the TE-TM mode spacing decreases for smaller refractive index contrasts. Decreasing the refractive index contrast increased the linewidth of the resonances because the resonance quality factor of the mode is lower. We measured a quality factor of approximately $8 \cdot 10^3 \pm 2 \cdot 10^3$ for the TE_{96} mode in a polystyrene microsphere immersed in water, the contrast in index of refraction being 1.195. Decreasing the contrast in index of refraction to 1.137 ($m_0 = 1.3978$) we found a resonance quality factor of approximately 750 ± 100.

The curves for the full width half maximum and the TE-TM mode spacing were fitted with theoretical curves. The theoretical values for the linewidth and mode spacing were obtained from the poles of the scattering coefficients. The theoretical curves showed excellent agreement with the experimental results we obtained.

We also performed measurements on the dye doped polystyrene microspheres using pulsed laser excitation. The pulsed laser excitation reached a peak power about 60 times higher than continuous wave excitation. Under pulsed laser excitation we observed single mode as well as multi-mode lasing in the emission spectrum of the dye. The number of laser lines strongly depended on the sphere size, sphericity and surface roughness of the microsphere and could not be predicted on forehand. Due to stimulated emission in the microsphere the intensity of the natural modes was up to 30 times higher than the fluorescent background. We observed a lasing threshold for all the laser lines in the emission spectrum and determined the threshold luminance.

Using Mie theory with gain in the refractive index we theoretically determined the gain in the microsphere of the TE_{95} and TM_{95} modes for a pump power on and above threshold. The gain for the TE_{95} mode corresponds to $\mathrm{Im}(m_I) = 3.9 \cdot 10^{-5}$ when the mode is in a lasing condition. The TM_{95} mode needs a higher gain in order to pass the threshold because it has a higher loss factor. At and above threshold it has a gain of $\mathrm{Im}(m_I) = 5.1 \cdot 10^{-5}$.

5.2 Recommendations for further research

Several ideas we have for upcoming experiments and new theoretical considerations are listed here.

1. A fairly easy aspect to implement in the theory for the fluorescence of dipoles in a spherical cavity is the excitation strength of the dipoles. This is not considered in the model as described in this thesis. An incoming excitation laser beam will create an electromagnetic field distribution inside the spherical cavity. This distribution is described by the Mie theory. The consequence is that certain dipoles will be in a region where the intensity of the electromagnetic field is higher. The dipoles feeling a higher field intensity feel a higher excitation strength. We expect the effect on the final result to be small. The incoming laser beam will not have a frequency corresponding to a resonance frequency of the microsphere. Therefore the electromagnetic field distribution in the cavity is more or less constant.

2. An experiment which is fairly easy to perform is measuring the emission spectrum of very large ($\sim 100\mu$m) dye doped polystyrene microspheres. The free spectral range of the resonances in these spheres is ten times smaller than the 10 μm microspheres we measured on. This results in more resonances in the spectral range of the spectrograph. Using these bigger microspheres it is easier to perform statistics on lasing resonances. For example the number of modes which are laser modes can be evaluated. Also the observation that TE modes are more often laser modes than TM modes can be verified.

3. Experimentally it should be possible to measure a lasing threshold in the full width at half maximum of a lasing resonance. Therefore a high resolution (small pixel size) spectrograph is needed. An estimation of the resolution needed is 0.002 nm/pixel to be able to see the change in full width at half maximum when passing the lasing threshold.

4. A very interesting next step in the experimental research described in this thesis is the analysis of fluorescence from two or more microspheres placed in each others vicinity. The two microspheres need to be on resonance to be able to couple to each other. This means they need to have the same overlapping eigenfrequencies, and thus have the same size parameter x. This can be simpler when the contrast in index of refraction is low, which means the resonances are much wider and will overlap even if the spheres are not exactly the same size.

   The overlap of resonances will induce a split in the eigenmodes of the system [48, 49]. One narrow single sphere resonance splits in two broader bi-sphere resonances. It is also possible that, due to negative feedback between the two spheres, single sphere resonances are suppressed.

   A sphere size between 5 and 10 μm seems to be the best size to do these experiments. These spheres have enough dye molecules to be able to detect the emission spectrum and the free spectral range is sufficient to prevent coupling between two modes with a different mode number. Also the spheres are small enough to have a sufficiently high trap stiffness. With a low trap stiffness it will not be possible to stably trap two spheres using timesharing.

   Pumping the bi-sphere with high power pulsed laser could induce lasing in the bi-sphere [50]. Interesting questions are whether the bi-sphere has a lower lasing threshold or shows lasing in other modes than a single microsphere. Another interesting measurement is the determination of the lasing threshold as a function of the distance between the two spheres.

Appendix A

Mie theory: The complete derivation

The rigorous solution for scattering of a plane wave on a spherical particle of arbitrary size is treated [4–6]. We start with the four independent Maxwell equations (section A.1) and derive the vector Helmholtz equation. Next step is to solve the vector Helmholtz equation which is done in section A.2. The boundary conditions of the problem are determined by applying Stokes' theorem to the first two Maxwell equations (section A.3). After expanding the incoming plane wave into spherical harmonics we can insert the boundary conditions in the solution of the vector Helmholtz equation and solve for the coefficients. This procedure is performed in section A.4. We now have the exact fields inside and outside the sphere. From these fields the amplitude functions (section A.5) and the scattering, extinction and absorption efficiency (section A.6) are derived.

A.1 Maxwell Equations

Start from the four independent Maxwell Equations:

$$\nabla \times \mathbf{H} = \frac{4\pi \mathbf{I}}{c} + \frac{1}{c}\frac{d\mathbf{D}}{dt} \tag{A.1}$$

$$\nabla \times \mathbf{E} = -\frac{1}{c}\frac{d\mathbf{H}}{dt} \tag{A.2}$$

$$\nabla \cdot \mathbf{I} + \frac{d\rho}{dt} = 0 \tag{A.3}$$

$$\nabla \cdot \mathbf{H} = 0 \tag{A.4}$$

$$\text{with } \mathbf{D} = \varepsilon \mathbf{E} \text{ and } \mathbf{I} = \sigma \mathbf{E}$$

where t is the time, c the speed of light, $\mathbf{H}$ the magnetic field strength, $\mathbf{E}$ the electric field strength, $\mathbf{D}$ the dielectric displacement, $\mathbf{I}$ the current density, ε the dielectric constant and σ is the conductivity.

Now we only consider periodic phenomena with a circular frequency of ω. All quantities will be written as complex functions of the time t in the form:

$$A = (\alpha + i\beta)e^{i\omega t}$$

Taking the time-derivative:

$$\frac{d}{dt}\mathbf{A} = i\omega(\alpha + i\beta)e^{i\omega t} = i\omega \mathbf{A} \tag{A.5}$$

Due to the periodicity of the considered phenomena the first two Maxwell equations simplify to (with $\mathbf{I} = \sigma\mathbf{E}$ and $\mathbf{D} = \varepsilon\mathbf{E}$):

$$\begin{aligned} \nabla \times \mathbf{H} &= \frac{4\pi\sigma}{c}\mathbf{E} + \frac{\varepsilon}{c}\frac{d\mathbf{E}}{dt} = \mathbf{E}\left(\frac{4\pi\sigma}{c} + \frac{\varepsilon i\omega}{c}\right) = ik\mathbf{E}\left(\frac{4\pi\sigma}{i\omega} + \varepsilon\right) \\ &= ikm^2\mathbf{E} \end{aligned} \tag{A.6}$$

$$\nabla \times \mathbf{E} = -\frac{1}{c}\frac{d\mathbf{H}}{dt} = -\frac{i\omega}{c}\mathbf{H} = -ik\mathbf{H} \tag{A.7}$$

with $k = \frac{\omega}{c} = \frac{2\pi}{\lambda}$ the propagation constant in vacuum and $m^2 = \varepsilon - \frac{i4\pi\sigma}{\omega}$ complex refractive index of the medium at frequency ω.

Now take the the curl of both equation (A.6) and (A.7). The curl of equation (A.6) gives:

$$\begin{aligned}
\nabla \times (\nabla \times \mathbf{H}) &= \nabla \times (ikm^2\mathbf{E}) \\
\nabla \times (\nabla \times \mathbf{H}) \equiv \nabla(\nabla \cdot \mathbf{H}) - \nabla^2\mathbf{H} &= -\nabla^2\mathbf{H} = -\Delta\mathbf{H} \\
\text{if the medium is homogeneous:} & \\
\nabla \times (ikm^2\mathbf{E}) = ikm^2(-ik\mathbf{H}) &= k^2m^2\mathbf{H} \\
\Delta\mathbf{H} &= -k^2m^2\mathbf{H}
\end{aligned} \tag{A.8}$$

The curl of equation (A.7) gives:

$$\begin{aligned}
\nabla \times (\nabla \times \mathbf{E}) &= \nabla \times (-ik\mathbf{H}) \\
\text{if the medium is homogeneous, } \nabla \cdot \mathbf{D} &= 4\pi\rho = 0 \\
\text{then: } \nabla \cdot \mathbf{E} = 0,\ \nabla \times (\nabla \times \mathbf{E}) &= -\Delta\mathbf{E} \\
\nabla \times (-ik\mathbf{H}) = -ik(\nabla \times \mathbf{H}) &= -ikikm^2\mathbf{E} = k^2m^2\mathbf{E} \\
\Delta\mathbf{E} &= -k^2m^2\mathbf{E}
\end{aligned} \tag{A.9}$$

Equations (A.8) and (A.9) are vector Helmholtz equations. These curls show that for a homogeneous medium any rectangular component of $\mathbf{E}$ or $\mathbf{H}$ satisfies the scalar wave equation $\Delta\psi = -k^2m^2\psi$.

A.2 Solution of the vector Helmholtz equation

In order to solve the vector Helmholtz equation (equation (A.9)) we start from the scalar Helmholtz equation:

$$\nabla^2\psi + k^2m^2\psi = 0 \tag{A.10}$$

The scalar Helmholtz equation can be solved by separating variables, which yields as elementary solutions [51]:

$$\psi_{ln}(r,\theta,\phi) = \begin{cases} \cos(l\phi) \\ sin(l\phi) \end{cases} \quad P_n^l(cos\theta)z_n(mkr) \tag{A.11}$$

with n and l integers which satisfy $n \geq l \geq 0$ and the third factor a spherical Bessel function :

$$z_n(x) = \sqrt{\frac{\pi}{2x}}J_{n+\frac{1}{2}}(x) \quad or \quad \sqrt{\frac{\pi}{2x}}Y_{n+\frac{1}{2}}(x)$$

also denoted as

$$z_n(x) = j_n(x) \quad or \quad n_n(x)$$

The general solution of (A.10) is a linear combination of these elementary solutions (A.11).

Now suppose that we construct a vector function $\mathbf{M}$ from a scalar function ψ and the radius vector $\mathbf{r}$:

$$\mathbf{M}_\psi = \nabla \times (\mathbf{r}\psi)$$

As Bohren and Huffman [52] show, the vector function $\mathbf{M}_\psi$ satisfies the vector Helmholtz equation (equation (A.9)) in spherical coordinates if ψ is a solution to the scalar Helmholtz equation. We can also construct $\mathbf{M}_\psi$ from another vector function:

$$\mathbf{N}_\psi = \frac{\nabla \times \mathbf{M}_\psi}{mk}$$

which also satisfies the vector Helmholtz equation. $\mathbf{M}$ and $\mathbf{N}$ are connected by

$$mk\mathbf{M}_\psi = \nabla \times \mathbf{N}_\psi$$

Now let u and v be two solutions to equation (A.10), it is easy to show that

$$\mathbf{E} = \mathbf{M}_v + i\mathbf{N}_u \tag{A.12}$$

$$\mathbf{H} = m(-\mathbf{M}_u + i\mathbf{N}_v) \tag{A.13}$$

are solutions of the Maxwell equations (A.6) and (A.7).

We can summarize that finding solutions to the vector Helmholtz equation reduces to the simpler problem of finding two solutions to the scalar Helmholtz equation. The scalar function ψ is often called a *generating function* for the vector harmonics $\mathbf{M}$ and $\mathbf{N}$.

A.3 Boundary Conditions

Consider a sharp boundary between two homogeneous media with refractive indices m_1 and m_2 respectively. The values of m_1 and m_2 are assumed to be finite. Let $\mathbf{n}$ be the normal to the boundary surface, directed into medium m_2. We can now use the well known Stokes' theorem (see for example [53]) given by:

$$\int_{surface} (\nabla \times \mathbf{v}) \cdot d\mathbf{a} = \oint_{boundary\ line} \mathbf{v} \cdot d\mathbf{l} \tag{A.14}$$

Starting from equation (A.6) the first boundary condition follows with the use of Stokes' theorem. Starting with the left hand side:

$$\int_{surface} (\nabla \times \mathbf{H}) \cdot d\mathbf{a} = \oint_{boundary\ line} \mathbf{H} \cdot d\mathbf{l} = H_{2//} - H_{1//} = \mathbf{n} \times (\mathbf{H_2} - \mathbf{H_1})$$

Using a limiting process for the right hand side of equation (A.6):

$$0 \leq \mid \int_{surf} (ikm^2\mathbf{E}) \cdot d\mathbf{a} \mid \leq \int_{surf} \mid km^2 \mid\mid \mathbf{E} \cdot d\mathbf{a} \mid \leq \int_{surf} \mid km^2 \mid max \mid \mathbf{E} \mid S \tag{A.15}$$

with S $\downarrow$ 0, m and $\mathbf{E}$ finite it follows

$$\mathbf{n} \times (\mathbf{H_2} - \mathbf{H_1}) = 0 \tag{A.16}$$

The second boundary condition follows from equation A.7 with once more Stokes' theorem. Using the same procedure as is used for the first boundary condition it follows that:

$$\mathbf{n} \times (\mathbf{E_2} - \mathbf{E_1}) = 0 \tag{A.17}$$

A.4 Solution of coefficients from boundary conditions

Now consider the scattering of a plane wave by a homogeneous sphere. We assume that the outside medium has refractive index m_0 and the inside medium (the sphere) has a refractive index of m_I. In order to simplify the calculations, the incident radiation is linearly polarized (electric field in the x-direction). Furthermore, the origin of our system is chosen at the center of the sphere with the positive z-axis along the direction of the propagation of the incident wave and the x-axis in the plane of electric vibration

of the incident wave. The incident wave is then described by

$$\mathbf{E} = \mathbf{1}_x e^{-ikm_0 z + i\omega t}$$
$$\mathbf{H} = \mathbf{1}_y e^{-ikm_0 z + i\omega t}$$

The plane wave expansion into spherical harmonics is done by setting [51]:

Outside incident wave

$$u = e^{i\omega t}\cos\phi \sum_{n=1}^{\infty} m_0(-i)^n \frac{2n+1}{n(n+1)} P_n^l(\cos\theta) j_n(m_0 kr)$$
$$v = e^{i\omega t}\sin\phi \sum_{n=1}^{\infty} m_0(-i)^n \frac{2n+1}{n(n+1)} P_n^l(\cos\theta) j_n(m_0 kr)$$

as u and v.

This form for the incident wave reveals how the wave functions corresponding to the complete solution look. From a consideration of the boundary conditions and the conditions to be satisfied at infinity, we can write :

Outside scattered wave:

$$u = e^{i\omega t}\cos\phi \sum_{n=1}^{\infty} -a_n m_0(-i)^n \frac{2n+1}{n(n+1)} P_n^l(\cos\theta) h_n^{(2)}(m_0 kr)$$
$$v = e^{i\omega t}\sin\phi \sum_{n=1}^{\infty} -b_n m_0(-i)^n \frac{2n+1}{n(n+1)} P_n^l(\cos\theta) h_n^{(2)}(m_0 kr)$$

Inside wave

$$u = e^{i\omega t} cos\phi \sum_{n=1}^{\infty} c_n m_I(-i)^n \frac{2n+1}{n(n+1)} P_n^l(cos\theta) j_n(m_I kr)$$
$$v = e^{i\omega t} sin\phi \sum_{n=1}^{\infty} d_n m_I(-i)^n \frac{2n+1}{n(n+1)} P_n^l(cos\theta) j_n(m_I kr)$$

Note that for the outside scattered wave the function $h_n^{(2)} = j_n - in_n$ is chosen instead of j_n due to its asymptotic behavior for large r

$$h_n^{(2)}(m_0 kr) \sim \frac{i^{n+1} e^{-im_0 kr}}{m_0 kr} \tag{A.18}$$

All series contain elementary solutions for $l = 1$ only due to the orthogonality of the

higher order functions. We now only need to derive the coefficients c_n, d_n, a_n and b_n from the boundary conditions (A.16) and (A.17) in order to find the total magnetic and electric field. We see from these conditions that only the non-radial part of **E** and **H** is important here. We have from (A.16) and (A.17):

$$(\mathbf{E_i} + \mathbf{E_s} - \mathbf{E_I})\mathbf{e_r} = (\mathbf{H_i} + \mathbf{H_s} - \mathbf{H_I})\mathbf{e_r} = 0$$

Only the radial part is of interest to us:

$$\begin{aligned} E_{i\theta} + E_{s\theta} &= E_{I\theta} \\ E_{i\phi} + E_{s\phi} &= E_{I\phi} \\ H_{i\theta} + H_{s\theta} &= H_{I\theta} \\ H_{i\phi} + H_{s\phi} &= H_{I\phi} \end{aligned}$$

where i denotes incoming, s the scattered and I the internal part of the electromagnetic field. Solving the real and imaginary parts of these equations gives us:

$$v_i + v_s = v_I$$

$$\frac{1}{m_0 k}\left(\frac{\delta^2(ru_i)}{\delta r \delta\theta} + \frac{\delta^2(ru_s)}{\delta r \delta\theta}\right) = \frac{1}{m_I k}\frac{\delta^2(ru_I)}{\delta r \delta\theta}$$

$$m_0(u_i + m_s) = m_I u_I$$

$$\frac{\delta(rv_i)}{\delta r} + \frac{\delta(rv_s)}{\delta r} = \frac{\delta(rv_I)}{\delta r}$$

Expressions for the coefficients become far easier when using the Riccati-Bessel functions:

$$\psi_n(z) = zj_n(z), \chi_n(z) = -zn_n(z), \zeta_n(z) = zh_n^{(2)}(z)$$

and since

$$H_n^{(2)}(z) \quad = J_n(z) - iN_n(z)$$

we have

$$\zeta_n(z) \quad = \psi_n(z) + i\chi_n(z)$$

We put

$$x = m_0 ka = \frac{2\pi m_0 a}{\lambda} \ , \ y = m_I ka$$

The variable x is the size parameter of the system. It depends on the size of the particle and on the wavelength of the incoming wave. We now have as boundary conditions :

$$\begin{aligned}
\psi_n(x) - b_n\zeta_n(x) &= d_n\psi_n(y) \\
\psi_n^{'}(x) - a_n\zeta_n^{'}(x) &= c_n\psi_n^{'}(y) \\
m_0[\psi_n(x) - a_n\zeta_n(x)] &= m_I c_n\psi_n(y) \\
m_0[\psi_n^{'}(x) - b_n\zeta_n^{'}(x)] &= m_I d_n\psi_n^{'}(y)
\end{aligned}$$

We now have 4 equations which give the expressions for the coefficients:

The coefficients for the field outside the sphere (scattering coefficients):

$$a_n = \frac{m_0\psi_n'(y)\psi_n(x) - m_I\psi_n(y)\psi_n'(x)}{m_0\psi_n'(y)\zeta_n(x) - m_I\psi_n(y)\zeta_n'(x)}$$

$$b_n = \frac{m_I\psi_n'(y)\psi_n(x) - m_0\psi_n(y)\psi_n'(x)}{m_I\psi_n'(y)\zeta_n(x) - m_0\psi_n(y)\zeta_n'(x)}$$

The coefficients for the field inside the sphere:

$$c_n = \frac{m_0(\psi_n'(x)\zeta_n(x) - \zeta_n'(x)\psi_n(x))}{m_0\psi_n'(y)\zeta_n(x) - m_I\psi_n(y)\zeta_n'(x)}$$

$$d_n = \frac{m_0(\psi_n'(x)\zeta_n(x) - \zeta_n'(x)\psi_n(x))}{m_I\psi_n'(y)\zeta_n(x) - m_0\psi_n(y)\zeta_n'(x)}$$

Note that a_n and b_n vanish for $m_I = m_0$; this is as it should be: when the particle disappears so does the scattered field.

Having derived the coefficients for the scalar waves inside and outside the sphere the Mie problem is solved. The generating functions are known, and using equations (A.12) and (A.13) we can calculate the vector fields inside and outside the Mie sphere. The vector fields inside and outside the sphere give the full rigorous solution. Quantities like the amplitude functions and the efficiencies for scattering and extinction can be derived from these fields.

A.5 Outside solution: Amplitude functions

The Mie solution sketched in the previous sections gives the fields at any point inside and outside the particle. Now look at the scattered field far from the sphere ($r = \sqrt{x^2+y^2+z^2} \approx z$). We can substitute the asymptotic expression for $h_n^{(2)}$ (equation

(A.18)):

$$u = \frac{-i}{kr} e^{-im_0 kr + i\omega t} \cos\phi \sum_{n=1}^{\infty} a_n \frac{2n+1}{n(n+1)} P_n^1(\cos\theta)$$
$$v = \frac{-i}{kr} e^{-im_0 kr + i\omega t} \sin\phi \sum_{n=1}^{\infty} b_n \frac{2n+1}{n(n+1)} P_n^1(\cos\theta)$$

Now derive the components of $\mathbf{E}$ and $\mathbf{H}$ using the above expressions for u and v and equations (A.12) and (A.13). The result is:

$$E_\theta^{sca} = H_\phi^{sca} = \frac{-i}{kr} e^{-im_0 kr + i\omega t} \cos\phi S_2(\theta) \tag{A.19}$$
$$-E_\phi^{sca} = H_\theta^{sca} = \frac{-i}{kr} e^{-im_0 kr + i\omega t} \sin\phi S_1(\theta) \tag{A.20}$$
$$E_r^{sca} = H_r^{sca} = 0 \tag{A.21}$$

with the amplitude functions:

$$S_1(\theta) = \sum_{n=1}^{\infty} \frac{2n+1}{n(n+1)} [a_n \pi_n(\cos\theta) + b_n \tau_n(\cos\theta)] \tag{A.22}$$
$$S_2(\theta) = \sum_{n=1}^{\infty} \frac{2n+1}{n(n+1)} [b_n \pi_n(\cos\theta) + a_n \tau_n(\cos\theta)] \tag{A.23}$$

where π_n and τ_n are functions of the P_n^1 Legendre polynomials:

$$\pi_n(\cos\theta) = \frac{1}{\sin\theta} P_n^1(\cos\theta) \tag{A.24}$$
$$\tau_n(\cos\theta) = \frac{d}{d\theta} P_n^1(\cos\theta) \tag{A.25}$$

We now have the amplitude functions which are used to derive the extinction, scattering and absorption efficiencies.

A.6 Efficiency factors

A.6.1 Extinction

Most particles have an obvious geometrical cross section G. A sphere of radius a has, for instance, $G = \pi a^2$. The dimensionless constants

$$Q = \frac{C}{G}$$

will be called the *efficiency factors*. These factors can be defined for scattering, extinction and absorption. C is the optical cross section of the particle. The efficiency factor for extinction may be determined from the amplitude function for $\theta = 0$. For $\theta = 0$ and $\theta = 180$ the coefficients are independent of the polarization state of the incoming wave because $S_1(\theta)$ and $S_2(\theta)$ are equal (and thus indistinguishable). In other directions the scattering plane enforces a distinction. Both $S_1(\theta)$ and $S_2(\theta)$ have the value

$$S(0) = \frac{1}{2}\sum_{n=1}^{\infty}(2n+1)(a_n + b_n)$$

The value of Q_{ext} follows from [51]:

$$C_{ext} = \pi a^2 Q_{ext} = \frac{4\pi}{m_0^2 k^2} Re[S(0)] \tag{A.26}$$

so that

$$Q_{ext} = \frac{4}{x^2} Re[S(0)]$$

Expressed in Mie-coefficients the extinction cross section and -efficiency read

$$C_{ext} = \frac{2\pi}{m_0^2 k^2}\sum_{n=1}^{\infty}(2n+1)Re(a_n + b_n) \tag{A.27}$$

$$Q_{ext} = \frac{2}{x^2}\sum_{n=1}^{\infty}(2n+1)Re(a_n + b_n) \tag{A.28}$$

A.6.2 Scattering

In order to calculate the scattering cross section and -efficiency we introduce a function $F(\theta, \phi)$ which defines the intensity of the scattered light in an arbitrary direction:

$$I = \frac{I_0 F(\theta, \phi)}{m_0^2 k^2 r^2}$$

For linearly polarized light we have:

$$F(\theta,\phi) = |S_1(\theta)|^2 \cos^2(\phi) + |S_2(\theta)|^2 \sin^2(\phi)$$

Now let the total energy scattered in all directions be equal to the energy of the incident wave falling on the area C_{sca}. By this definition we have

$$C_{sca} = \frac{1}{m_0^2 k^2} \int F(\theta,\phi) d\omega$$

Where $d\omega$ denotes the solid angle. So integrating over all angles gives

$$C_{sca} = \frac{1}{m_0^2 k^2} \int_0^{\pi} \int_0^{2\pi} (|S_1(\theta)|^2 \cos^2(\phi) + |S_2(\theta)|^2 \sin^2(\phi)) \sin(\theta) d\phi d\theta \tag{A.29}$$

After subsitution we have

$$C_{sca} = \frac{2\pi}{m_0^2 k^2} \sum_{n=1}^{\infty} (2n+1)(|a_n|^2 + |b_n|^2) \tag{A.30}$$

$$Q_{sca} = \frac{C_{sca}}{\pi a^2} = \frac{2}{x^2} \sum_{n=1}^{\infty} (2n+1)(|a_n|^2 + |b_n|^2) \tag{A.31}$$

A.6.3 Absorption

Since by definition we have

$$Q_{ext} = Q_{sca} + Q_{abs}$$

Q_{abs} can be calculated from Q_{ext} and Q_{sca}.

Bibliography

[1] F. Vollmer, D. Braun, A. Libchaber, M. Khoshsima, I. Teraoka, and S. Arnold. Protein detection by optical shift of a resonant microcavity. *Appl. Phys. Lett.*, **80**:4057–4059, 2002.

[2] SL Hale, KJ Alker, and RA Kloner. Evaluation of nonradioactive, colored microspheres for measurement of regional myocardial blood flow in dogs. *Circulation*, **78**:428–434, 1988.

[3] K.J. Vahala. Optical microcavities. *Nature*, **424**:839–846, 2003.

[4] G. Mie. Beitrage zur Optik trüber Medien, speziell kolloidaler Metallösungen. *Ann. Physik*, **25**:337–445, 1908.

[5] C.F. Bohren, and D.R. Huffman. *Absorption and Scattering of Light by Small Particles*. John Wiley and Sons, Inc., New York, 1983.

[6] H.C. van de Hulst. *Light scattering by Small Particles*. Dover Publications, Inc., New York, 1981.

[7] N.G. Alexopoulos, and N.K. Uzunoglu. Electromagnetic scattering form active objects: invisible scatterers. *Appl. Opt.*, **17**:235–239, 1978.

[8] M. Kerker. Electromagnetic scattering from active objects. *Appl. Opt.*, **17**:3337–3339, 1978.

[9] M. Kerker. Resonances in electromagnetic scattering by objects with negative absorption. *Appl. Opt.*, **18**:1180–1189, 1979.

[10] H.S. Bennet. Resonances in the efficiency factors for absorption: Mie scattering theory. *Appl. Opt.*, **17**:491–493, 1978.

[11] C.C. Lam, P.T. Leung, and K. Young. Explicit asymptotic formulas for the positions, widths, and strengths of resonances in Mie scattering. *J. Opt. Soc. Am. B*, **9**:1585–1592, 1992.

[12] H.M. Lai, C.C. Lam, P.T. Leung, and K. Young. Effect of perturbations on the widths of narrow morphology-dependent resonances in Mie scattering. *J. Opt. Soc. Am. B*, **8**:1962–1973, 1991.

[13] A. Ashkin, and J. M. Dziedzic. Observation of Resonances in the Radiation Pressure on Dielectric Spheres. *Phys. Rev. Lett*, **38**:1351–1354, 1977.

[14] R.E. Benner, P.W. Barber, J.F. Owen, and R.K. Chang. Observation of Structure Resonances in the Fluorescence Spectra from Microspheres. *Phys. Rev. Lett.*, **44**:475–478, 1980.

[15] S. Holler, N.L. Goddard, and S. Arnold. Spontaneous emission spectra from microdroplets. *J. Chem. Phys.*, **108**:6545–547, 1998.

[16] H. Chew. Transition rates of atoms near spherical surfaces. *J. Chem. Phys.*, **87**:1355–1360, 1987.

[17] H. Chew. Radiation and lifetimes of atoms inside dielectric particles. *Phys. Rev. A*, **38**:3410–3416, 1988.

[18] H.-M. Tzeng, K.F. Wall, M.B. Long, and R.K. Chang. Laser emission from individual droplets at wavelengths corresponding to morphology-dependent resonances. *Opt. Lett.*, **9**:499–501, 1984.

[19] S.X. Qian, J.B. Snow, H.-M. Tzeng, and R.K. Chang. Lasing droplets - highlighting the liquid-air interface by laser-emission. *Science*, **231**:486–488, 1986.

[20] H.-B. Lin, J.D. Eversole, and A.J. Campillo. Spectral properties of lasing microdroplets. *J. Opt. Soc. Am. B*, **9**:43–50, 1992.

[21] M. Kuwata-Gonokami, K. Takeda, H. Yasuda, and K. Ema. Laser emission from dye-doped polystyrene microsphere. *Jap. J. Appl. Phys.*, **31**:L99–L101, 1992.

[22] V. Sandoghdar, F. Treussart, J. Hare, V. Lefèvre-Seguin, J.-M. Raimond, and S. Haroche. Very low threshold whispering-gallery-mode microsphere laser. *Phys. Rev. A*, **54**:R1777–R1780, 1996.

[23] M. Cai, O. Painter, K.J. Vahala, and P.C. Sercel. Fiber-coupled microsphere laser. *Opt. Lett.*, **25**:1430–1432, 2000.

[24] V.V. Datsyuk. Gain effects on microsphere resonant emission structures. *J. Opt. Soc. Am. B*, **19**:142–147, 2002.

[25] E. Hecht. *Optics*, pages 409–413. Addison Wesley Longman, Inc., London, third edition, 1987.

[26] H. Chew, P.J. McNulty, and M. Kerker. Model for Raman and fluorescent scattering by molecules embedded in small particles. *Phys. Rev. A*, **13**:396–404, 1976.

[27] I.D. Nikolov, and C.D. Ivanov. Optical plastic refractive measurements in the visible and near-infrared regions. *Appl. Opt.*, **39**:2067–2070, 2000.

[28] X. Ma, J.Q. Lu, R. Scott Brock, K.M. Jacobs, P. Yang, and X. Hu. Determination of complex refractive index of polystyrene microspheres from 370 to 1610 nm. *Phys. Med. Biol.*, **48**:4165–4172, 2003.

[29] D.R. Lide. *CRC Handbook of Chemistry and Physics*. CRC Press, Florida, 2004.

[30] J. Lekavich. Basics of Acousto-Optic Devices. *Lasers and Appl.*, pages 59–64, 1986.

[31] P.A. Gass, and J.R. Sambles. Angle-frequency relationship for a practical acousto-optic deflector. *Opt. Lett.*, **18**:1376–1378, 1993.

[32] A. Pralle, M. Prummer, E.-L. Florin, E.H.K. Stelzer, and J.K.H. Hörber. Three-dimensional High-Resolution Particle Tracking for Optical Tweezers by Forward Scattered Light. *Micr. Res. Tech.*, **44**:378–386, 1999.

[33] A. Rohrbach, and E.H.K. Stelzer. Three-dimensional position detection of optically trapped dielectric particles. *J. Appl. Phys.*, **91**:5474–5488, 2001.

[34] A. Ashkin, and J.M. Dziedzic. Optical Levitation by Radiation Pressure. *Appl. Phys. Lett.*, **19**:283–285, 1971.

[35] A. Ashkin. Acceleration and Trapping of Particles by Radiation Pressure. *Phys. Rev. Lett.*, **24**:156–159, 1970.

[36] A. Ashkin, J.M. Dziedzic, J.E. Bjorkholm, and S. Chy. Observation of a single-beam gradient force optical trap for dielectric particles. *Opt. Lett.*, **11**:288–291, 1986.

[37] A. Ashkin. History of optical trapping and manipulation of small-neutral particle, atoms, and molecules. *IEEE J. Sel. Top. Quantum Electron.*, **6**:841–856, 2000.

[38] K.C. Neuman, and S.M. Block. Optical trapping. *Rev. Sci. Instr.*, **75**:2787–2809, 2004.

[39] A. Ashkin. Forces of a single-beam gradient laser trap on a dielectric sphere in the ray optics regime. *Biophysical Journal*, **61**:569–582, 1992.

[40] K. Visscher, and G. J. Brakenhoff. Theoretical study of optically induced forces on spherical particles in a single beam trap II: Mie scatterers. *Optik*, **90**:57–60, 1992.

[41] K. F. Ren, G. Greha, and G.Gouesbet. Radiation Pressure Forces Exerted on a Particle Arbitrarily Located in a Gaussian-Beam by Using the Generalized Lorenz-Mie Theory, and Associated Resonance Effects. *Opt. Commun.*, **108**:343–354, 1994.

[42] K. Svoboda, and S.M. Block. Biological Applications of Optical Forces. *Ann. Rev. Biophys. Biomol. Struct.*, **23**:247–285, 1994.

[43] J. Bechhoefer, and S. Wilson. Faster, cheaper, safer optical tweezers for the undergraduate laboratory. *Am. J. Phys.*, **70**:393–400, 2001.

[44] M.L. Bennink. *Force spectroscopy of single DNA-protein complexes*. PhD thesis, University of Twente, Netherlands, 2001.

[45] R. Loudon. *The Quantum Theory of Light*, page 68. Oxford Univesity Press Inc., New York, third edition, 2000.

[46] E. Hecht. *Optics*, pages 115–118. Addison Wesley Longman, Inc., London, third edition, 1987.

[47] A.E. Siegman. *Lasers*, pages 323–324. University Science Books, Sausalito, California, 1986.

[48] K.A. Fuller. Optical resonances in two-sphere systems. *Appl. Opt.*, **30**:4716–4731, 1991.

[49] D.D. Smith, H. Chang, and K.A. Fuller. Whispering-gallery mode splitting in coupled microresonators. *J. Opt. Soc. Am. B*, **20**:1967–1974, 2003.

[50] Y. Hara, T. Mukaiyama, K. Takeda, and M. Kuwata-Gonokami. Photonic molecule lasing. *Opt. Lett.*, **28**:2437–2439, 2003.

[51] K.L. van der Molen, T. Savels, and P. Zijlstra. Rigorous scattering theory of spheres with arbitrary size. *Internal communication*, 2005.

[52] C.F. Bohren, and D.R. Huffman. *Absorption and Scattering of Light by Small Particles*, pages 83–89. John Wiley and Sons, Inc., New York, 1983.

[53] D.J. Griffiths. *Introduction to Electrodynamics*, pages 31–36. Prentice Hall Inc., New Jersey, third edition, 1999.